



---

# Towards an interferometer with parametric amplifiers testing spontaneous wave function collapse

---

THESIS

submitted in partial fulfillment of the requirements for  
the degree of

MASTER OF SCIENCE

in

PHYSICS

Author : X. G. A. Le Large  
Student ID : XXXXXXXXXX  
Supervisor : Prof.dr.ir. T.H. Oosterkamp  
Daily Supervisor : T.H.A. van der Reep, Msc.  
2<sup>nd</sup> corrector : dr. W. Löffler

Leiden, The Netherlands, June 13, 2018



## Preface

After finding out about the existence of the strange world of quantum mechanics at the age of 14 in a library in Rotterdam, like many others, I was confused yet intrigued at the same time. It was certainly one of the ideas of modern physics that made me decide to study physics at Leiden University. Before starting, I spent three days at the Lorentz Institute as part of my final school project to observe the building of a Michelson interferometer by former PhD student Jelmer Renema and observe quantum interference of single photons myself. During my studies, it came as no surprise that wave function collapse, the reduction of a wave function describing a system with many quantum states to a single eigenstate, is still poorly understood. It is, however, a crucial element in the unification of quantum physics and general relativity.

This thesis describes the work done as part of a feasibility study of a proposed interferometric experiment, that is expected to falsify the existence of spontaneous wave function collapse. Next to quite challenging and diverse, ranging from quantum optics and thermodynamics to obtaining accounts for the national supercomputer facility, it has certainly been an instructive and interesting experience.

During this project, I have been supported by a number of people to whom I want to express my sincere gratitude and appreciation. First and foremost, my supervisors prof. Tjerk Oosterkamp and Tom van der Reep, who have given me the opportunity to take part in this project and have shown great patience during this research. Secondly, Ruben Guijs, who joined project as a BSc. student and proved to be a nice and helpful companion in the quest of calculating interference visibilities for a larger value of the infamous  $kappa$ . Thirdly, the excellent support of the following people: the Oosterkamp Group members and FMD for the nice working atmosphere and technical support for the cryogenic calorimeter; Leonardo Lenocil for setting up an account on the Maris Cluster of prof. Carlo Beenakker and answering all my questions, while he and the other users of the cluster tolerated my intensive use of its resources; prof. Portegies Zwart for bringing me into contact with the Dutch national high-performance computing support center SURFsara; Marco Verdicchio and Nuno Ferreira, IT consultants at SURFsara for their much appreciated support in discussing the possibilities of doing the computer calculations with more resources available and for setting up a user account on the High Performance Computing Cloud and the Lisa system; Paul Nation, one of the developers of the QuTiP module, for answering my questions on the GitHub forum, and Oliver Ostojić, who answered quite a few of MatLAB-related questions. Last but not least, I would like to thank my friends (especially Wouter, Bart and Fleur) for their moral support and of course my parents, who supported me in many ways during my studies at Leiden University.

I hope you will enjoy reading this thesis!

Xavier Le Large

*Leiden, June 13, 2018*



## Abstract

For a phenomenological explanation of the absence of macroscopic superpositions, mass-dependent non-linear and stochastic terms are added to the Schrödinger equation in some models of wave function collapse. This thesis describes a feasibility study of a microwave interferometer experiment with the purpose of falsifying the existence of spontaneous wave function collapse. Traveling wave parametric amplifiers in the interferometer arms effectively increase the mass of these superpositions, resulting in an interference visibility and an expected vanishing visibility in case of wave function collapse. The main question arises if the visibilities for these cases can be distinguished from each other in case of a gain of 20 dB and a (typical) insertion loss of 4 dB of the parametric amplifiers.

Calculations of the interference visibilities were extended and performed by a Python program with the QuTiP module by using a Master Equation solver and Monte Carlo simulations on different computer infrastructures with up to 1.5 TB of RAM available. The limitations of the solvers were the QuTiP internals and computational time respectively. Visibilities are calculated using the Master Equation solver for gains up to 13.4 dB when neglecting losses, and for gains up to 5.3 dB and insertion losses up to 6.5 dB when including the effect of dissipation using both solvers. The differences between both visibilities appear to converge to constant values in the limit of large gain. Further calculations can be carried out on the Lisa Cluster to explore this promising observation.

In addition, a cryogenic calorimeter for determining the insertion loss of an amplifier is characterized by its thermal time constants. Efforts were made to reduce the time constant attributed to a 3 dB attenuator, allowing for a precise determination of its power dissipation.

On the basis of the results of this study, it can be concluded that significant steps in determining the feasibility of the proposed interferometer experiment are taken and future research is encouraged.



# Table of Contents

Preface.....	1
Abstract .....	3
1 Introduction .....	7
2 Theory .....	8
2.1 Collapse of the wave function .....	8
2.1.1 Models of wave function collapse .....	8
2.1.2 Preview of the final experiment .....	9
2.2 Overview of the computer program .....	12
2.2.1 Master equation solver .....	13
2.2.2 Monte Carlo solver .....	14
2.3 Heat-loss compensated calorimeter .....	15
2.3.1 Heat transfer and calorimetry .....	15
2.3.2 From a thermal model to differential equations .....	17
3 Experimental setup & Methods .....	21
3.1 Cryogenic dual loss compensated calorimeter .....	21
3.2 Material properties and calculations on the three different experimental set-ups .....	22
3.3 Methods .....	28
4 Results & Discussion .....	29
4.1 Calculations excluding losses .....	29
4.1.1 ME solver .....	29
4.2 Calculations including losses .....	31
4.2.1 ME solver .....	31
4.2.2 MC solver .....	33
4.3 Thermal time constants .....	36
4.3.1 Run 75, 76 and 77 .....	36
5 Conclusion & Outlook .....	39
Bibliography .....	41
Appendix A: Computer Infrastructures .....	43
Appendix B: Quick start guide SLURM & Maris Cluster .....	45
Appendix C: Additional results .....	47



## 1 Introduction

Quantum theory is a highly successful conceptual framework about the origin of microscopic nature, both in fundamental and applied physics proven to be highly effective. However, this framework starts failing to hold when the time evolution of the mechanics of larger systems is considered, as expected for a 100 nm virus and shown for organic molecules with masses up to 6,910 AMU [1][2], and is even completely invalid for macroscopic systems, which have not been brought in a quantum superposition to date. The wave function, a mathematical description of a quantum state, is attributed to this superposition and hypothesized to collapse upon measurement [3]. The absence of macroscopic superpositions is a yet unexplained phenomenon and simultaneously an important unsolved problem concerning the interpretation of quantum mechanics.

Over the years, various explanations have been proposed to bridge the gap between quantum mechanics and general relativity, some of them suggesting that the fact that absence of macroscopic superposition indicates that the Schrödinger equation in this form is incomplete and needs to be modified [4]. All collapse models are based on the hypothesis of a spontaneous collapse of the wave function, where the presence of a superposition at the macroscopic level is theoretically possibly yet highly unlikely to subsist. With the number of constituents of a system as amplification mechanism for this rate of wave function collapse, an interferometric experiment proposed by Rademaker et al. [5] and described in [6] could be able to falsify the concept of spontaneous collapse. In short, traveling wave parametric amplifiers in this balanced microwave interferometer can effectively enlarge the mass of a superposition when their gain is increased. It is argued that if the process of spontaneous collapse exists, the visibility of the interference pattern will be reduced once the collapse process sets in. This deviation of the visibility between these scenarios may provide a hint for a mechanism that determines when the spontaneous collapse process sets in.

This thesis describes two preparatory experiments as part of a feasibility study of this proposed interferometric experiment. The first one concerns the numerical calculations of the magnitude of the interference visibility: can we distinguish the visibilities of the interference patterns of the two scenarios from each other in the case of a gain of 20 dB and an insertion loss of 4 dB of a traveling wave parametric amplifier? Before, this calculation has been performed for gains up to 11.6 dB when neglecting losses in the set-up and up to 1.8 dB in the presence of loss. Calculations for higher gain failed due to computer memory issues. Using different computers with more memory, we want to study calculate the interference visibilities for higher gains.

The second experiment consists of measurements on the thermal time constants of components in a calorimeter, in particular that of a 3 dB microwave attenuator, which we consider as comparable to the amplifier regarding its loss. Determining these allows one to calculate the power resolution of the calorimeter, which make accurate measurements of the power dissipation of the parametric amplifier possible. It is linked by the first experiment by the expectation that the power dissipation of the parametric amplifier is a considerable part of the insertion loss in the set-up, which reduces the interference visibility. Combining both experiments, a step towards conducting the interferometric experiment is taken.

The structure of this thesis is as follows. In each of the chapters, the calculations of the interference visibilities and the performance of the cryogenic calorimeter are treated subsequently. Chapter 2 starts with a review of wave function collapse models and the proposed interferometric experiment, continues with an explanation of the computer calculations and ends with a description of heat transfer within the calorimeter. Thereafter, the experimental set-up of the calorimeter is discussed in detail in chapter 3, while the methods used to obtain the computational results are provided in appendix B. Then, in chapter 4, the obtained results of the calculations of the interference visibilities and the measurements of the thermal time constants are presented and discussed simultaneously. Finally, the conclusions of both experiments are stated in chapter 5, which ends with an outlook to further research on this topics.

## 2 Theory

In this chapter, we will discuss and develop the theory that forms the starting point of our experiments. The first section (2.1) concerns the collapse of the wave function and the goal of the final experiment, motivating our experiments. The quantum optics involved here is intended to give the reader an introduction to the physics of the experiment as implemented in the computer program. It is important to study the attainable visibility for such a interferometric experiment. Therefore, section 2.2 describes the two solvers used in the computer program to calculate the interference visibilities. In the last section, 2.3, the cryogenic loss-compensated calorimeter is discussed and the heat flow equations specific to our experimental set-up are presented.

### 2.1 Collapse of the wave function

#### 2.1.1 Models of wave function collapse

Collapse models modify the Schrödinger equation by adding the collapse of the wave function to the standard quantum evolution. The origin of this collapse is yet unknown, but hypothesized to be the coupling to a noise field or gravity [7][8]. In its most basic form, the fundamental dynamics for the wave function in these models is given by the following stochastic differential equation [4]:

$$\frac{d|\psi(t)\rangle}{dt} = \left[ \frac{-i}{\hbar} \hat{H} + \sqrt{\lambda} (\hat{A} - \langle \hat{A} \rangle_t) \frac{dW_t}{dt} - \frac{\lambda}{2} (\hat{A} - \langle \hat{A} \rangle_t)^2 \right] |\psi_t\rangle, \quad (2.1)$$

where  $H$  is the quantum Hamiltonian of the system,  $\lambda$  is the (positive) collapse rate that sets the strength of the collapse mechanism,  $\hbar$  is the reduced Plank's constant,  $\langle A \rangle_t = \langle \psi_t | A | \psi_t \rangle$  is the expectation value of the operator  $A$ , here assumed to be self-adjoint and  $W_t$  is a standard Wiener process (the mathematical explanation of the stochastic one-dimensional Brownian motion). The second and third term on the RHS tend to collapse the wave function towards one of the eigenstates of the operator  $\hat{A}$  in a stochastic fashion. If these (nonlinear) collapse terms are dominant, the evolution of the wave function is stochastic and the wave function collapses very rapidly, eliminating the quantum behavior of a particle.

As these terms have negligible effects on the dynamics of microscopic systems, due to the deterministic evolution of their wave functions, but, at the same time their effects are strongly present for macroscopic objects, there must be an amplification mechanism. It has been proposed that the collapse strength of the center of mass is proportional to the number of constituents of the system [3]:

$$\lambda = \sum_{n=1}^N \lambda_n = \frac{M}{m_0} \lambda_0 \quad (2.2)$$

With this amplification mechanism, which is an important feature of collapse models, this equation allows one to describe quantum, mesoscopic and classical phenomena at the same time with a single choice of  $\lambda_0$ .

The most direct way of testing collapse models, which forbid the existence of macroscopic superpositions, is doing interferometric experiments [5]. Over the past years, larger masses have been brought into quantum superpositions for longer periods of time during which coherence is maintained in the experiment, after which the presence of quantum interference is detected [2][9]. In the next section, the interferometric experiment as proposed by Van der Reep and Oosterkamp [6] will be described, motivating the experiments done as part of a feasibility study during this master research project.

### 2.1.2 Preview of the final experiment

Here we discuss both the approach of the experiment that will be carried out in the future to falsify the spontaneous collapse of the wave function and the corresponding theory. Both parts of the discussion fully reflect the content of the research article about this experiment [6].

The set-up of this experiment consists of a microwave interferometer with a travelling wave parametric amplifier (TWPA) in each of its arms (fig. 2.1). First, single photons at GHz frequency are brought in a superposition by injecting them into a  $90^\circ$ -hybrid (the microwave analogue of a beam splitter). This entangles the amplifiers, which effectively enlarge the mass of the superposition (explained later on). After passing through a second  $90^\circ$ -hybrid, two detectors are used to measure the visibility of the interference pattern by measuring the number of signal and idler photons in each of the two output arms.

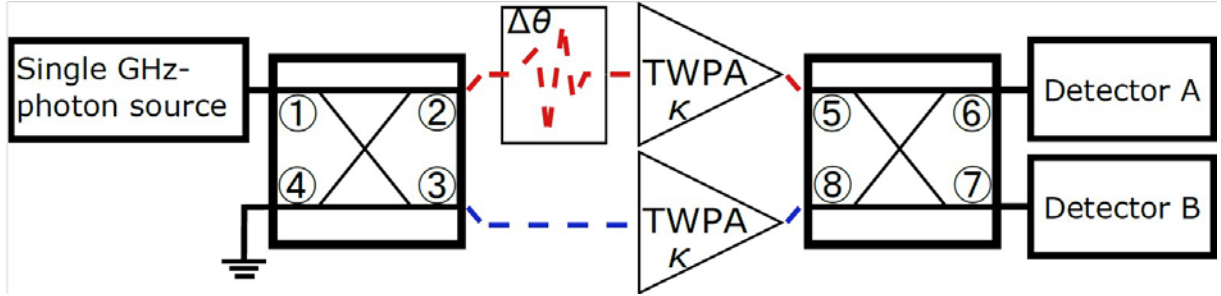


Figure 2.1. Schematic overview of the set-up of the final experiment as described in [6]. A single photon source is used to inject photons into a  $90^\circ$ -hybrid, where they are brought in a superposition of a single-photon input and a no-photon input. With the pump serving as energy source for the amplifications (characterized by  $\kappa$  and  $\kappa'$ , corresponding with a gain, and scaling with the pump power and photon frequency), the TPWAs effectively enlarge the mass of the superposition. The phase-shift  $\Delta\theta$  is assumed to account for all phase differences within the set-up. After recombining the photon currents in the second hybrid, the output radiation from arms 6 and 7 is measured in two detectors [6].

In this thesis, we do not provide an explanation for the effectively increased mass of the superposition by increasing the gain of the amplifiers in each of the arms of the interferometer. Using TPWAs, the entire set-up can microscopically be described by a single Hamiltonian, even when the gain of the amplifiers is increased. As we will not treat this balanced amplifier in detail, a short overview of its characteristics is given. It appears to be an appropriate tool in this microwave experiment due to its high gain and nearquantum limited noise, consisting of Josephson junctions [10]. In a four-wave mixing process, via frequency mixing such that  $2\omega_p = \omega_s + \omega_i$ , a signal and idler photon pair is created by annihilating two pump photons. The amplitude of the pump power is taken constant, the so-called undepleted pump approximation. A gain of 20 dB has been achieved for these devices [11].

We give an overview of the partial Hamiltonians in the set-up, i.e. for the  $90^\circ$ -hybrids, the phase shifters and the TPWAs. These Hamiltonians will be combined in the computer program (section 2.2) used to numerically evaluate the evolution of the wave function. This in turn makes it possible to compute the expectation values of the number of signal and idler photons in the output arms of the interferometer, after which the visibility of the resulting interference pattern can be calculated as well. We present the numerical implementations so that losses can be added straightforwardly to this model in section 2.2 [6].

As input state we take

$$|\psi\rangle = |1\rangle_{up,s} |0\rangle_{up,i} |0\rangle_{low,s} |0\rangle_{low,i}, \quad (2.3)$$

where the labels 'low' and 'up' refer to the lower arm and the upper arm of the interferometer respectively, and involve this by the time evolution operator,

$$|\psi(t + \Delta t)\rangle = e^{-\frac{iH_{int}\Delta t}{\hbar}} |\psi(t)\rangle, \quad (2.4)$$

in the interaction picture. By comparing this equation with the transformation operator for an ordinary 90°-hybrid,

$$\hat{U}_h = e^{\frac{i\pi}{4}(\hat{a}_{up,s}^\dagger \hat{a}_{low,s} + \hat{a}_{up,i}^\dagger \hat{a}_{low,i} + H.c.)}, \quad (2.5)$$

its Hamiltonian within this framework can effectively be described as

$$\hat{H}_h = \frac{-\hbar\pi}{4\Delta t_h} (\hat{a}_{up,s}^\dagger \hat{a}_{low,s} + \hat{a}_{up,i}^\dagger \hat{a}_{low,i} + H.c.), \quad (2.6)$$

with  $\Delta t_h$  being the time that the state spends in the hybrid.

By the same reasoning, the Hamiltonian for the phase shifter is given by

$$\hat{H}_{ps} = \frac{\hbar\Delta\theta}{\Delta t_{ps}} (\hat{a}_{up,s}^\dagger \hat{a}_{up,s} + \hat{a}_{up,i}^\dagger \hat{a}_{up,i}), \quad (2.7)$$

with  $\Delta\theta$  being the applied phase shift.

For the TWPA, we rewrite their Hamiltonian in the interaction picture,

$$\hat{H}_{TWPA} = \hbar\chi(\hat{a}_s^\dagger \hat{a}_i^\dagger \hat{a}_p^2 + H.c.), \quad (2.8)$$

describing the four-wave mixing process of creating a signal and idler photon pair by annihilating two pump photons (and vice versa) with a coupling constant  $\chi$ , to

$$\hat{H}^{up}_{TWPA} = \frac{\hbar\kappa_{up}}{\Delta t_{TWPA}} (\hat{a}_{up,s}^\dagger \hat{a}_{up,i}^\dagger + H.c.), \quad (2.9)$$

where the amplitude of the (coherent) pump is taken as a constant under the undepleted pump approximation and absorbed in a new coupling constant  $\chi'$ . For the numerical calculations (section 2.2), this has again been rewritten using  $\kappa = \chi' \Delta t_{TWPA}$  to parameterize the total gain of the amplifiers.

From the computed distribution of Fock states in the output arms 6 and 7 of the interferometer, the visibility of the interference pattern can be calculated in two manners. A large integration time of the photon detector results in measuring the average photon number, which gives an average visibility that can be defined as

$$V_{avg,s(i)} \equiv \frac{\langle n \rangle_{Bs(Ai)} - \langle n \rangle_{As(Bi)}}{\langle n \rangle_{Bs(Ai)} + \langle n \rangle_{As(Bi)}} \Big|_{\theta=0}. \quad (2.10)$$

Contrarily, single shot experiments done with an measurement apparatus with a short integration time result in a statistical visibility that can be defined as

$$V_{stat,s(i)} \equiv \frac{n_{Bs(Ai)} - n_{As(Bi)}}{n_{Bs(Ai)} + n_{As(Bi)}} \Big|_{\theta=0}. \quad (2.11)$$

The average photon number expected at the output of each of the TWPA's for both the signal and idler photons is

$$\langle n_{s(i),out} \rangle = \langle n_{s(i),in} \rangle \cosh^2 \kappa + (\langle n_{i(s),in} \rangle + 1) \sinh^2 \kappa. \quad (2.12)$$

Filling in  $\langle n_{i,in} \rangle = 0$  and  $\langle n_{s,in} \rangle = 0$  as number of input photons in eq. 2.12 and the resulting value of  $\langle n_{i,out} \rangle$  in eq. 2.10, it can be seen that the amplification  $\kappa$  can be translated into an experimentally comprehensible TWPA signal gain  $G$  can be calculated by

$$G(dB) = 10 \log_{10} \left( \frac{\langle n_{s,out} \rangle}{\langle n_{s,in} \rangle} \right) = 10 \log_{10} (\cosh^2(\kappa) + 2 \sinh^2(\kappa)), \quad (2.13)$$

where we have taken  $\langle n_{s,in} \rangle = \frac{1}{2}$  and  $\langle n_{i,in} \rangle = 0$  as input states. The factor 2 in front of the hyperbolic sine comes from dividing by the average signal photon number in the amplifiers, which is  $\frac{1}{2}$ .

Computer calculations on the signal and idler visibilities (as defined in eqs. (2.10) and (2.11)) have been carried out by Van der Reep to plot their magnitudes as a function of amplification when neglecting losses in the interferometer components. It is shown that the average idler visibility indeed has a constant value of  $1/3$ , while the average signal visibility decreases from 1 to 0.4 for  $\kappa = 1.5$ , tending to  $1/3$  as well for large amplification (fig. 2.2.).

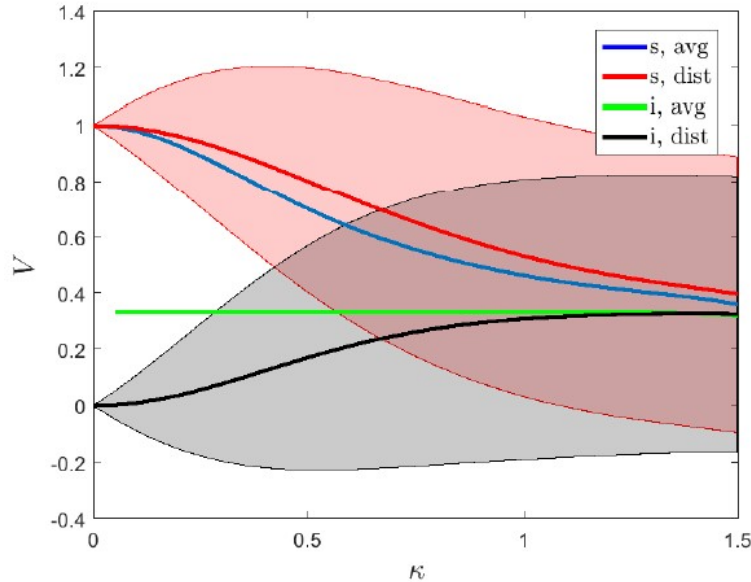


Figure 2.2. Expected visibilities of the interference pattern for signal (red) and idler (blue) photons as a function of amplification  $\kappa$  where losses in the components of fig. 2.1 are neglected. The average idler visibility has a constant value of  $1/3$ , while the signal visibility decreases from 1 to  $1/3$  for large amplification. Picture taken from [6].

For the statistical values of the visibilities the average value is plotted and the shaded areas gives the single shot  $1\sigma$ -confidence interval. The computer calculations will be treated in more detail in section 2.2. An important notion is the deviation of the calculated statistical idler visibility, which becomes larger than  $1/3$  (the magnitude of the average idler visibility) when the calculations are done for  $\kappa > 1.2$ . This is a strong indication that the program needs to run with different parameters and requires more computer resources. Figure 2.2 therefore marks the starting point of this part of the project.

Having introduced the visibility of the interference pattern that is expected for the proposed experiment, we now argue the importance of its magnitude. In order to be able to falsify the spontaneous continuous collapse model in the previous section, it is essential to make a distinction between the calculated visibilities as described above and those in the case of a collapse event. If the wave function collapses, the interference visibility is expected to decrease to zero.

The argument for this negative deviation in (signal) visibility is depicted in figure 2.3. For each state collapse, the exact opposite collapse occurs with the same probability according to the Wigner quasiprobability distribution (fig. 2.3, a). When a superposition of Fock states (with maximum phase uncertainty) collapses, we assume that it does so into classical coherent states with a well-defined phase (fig. 2.3, b). The output photon number in arms 6 and 7 is examined for two different scenarios as described below to argue what happens with the statistical and average (signal) visibilities in the case of wave function collapse (fig. 2.3, c).

In the case that these are the same (fig. 2.3, case i) ), the  $90^\circ$  phase shift of the hybrid causes the average photon number in arms 6 and 7 to be equal, resulting in  $V_{stat} = 0$  ( $V_{avg} = 0$  as well). When the wave function collapses into different coherent states (fig. 2.3, case ii), the individual collapses produce a visibility  $V_{stat} \neq 0$ . However, for each collapse, the exact opposite collapse occurs with the same probability according to the Wigner quasi-probability distribution. Hence, if the experiment is repeated, statistically  $V_{avg}$  and  $\langle V_{stat} \rangle$  will average out to 0. This reasoning is expected to hold for the case where

the effect of dissipation on the visibility is included as well, so that the question arises whether the magnitude of this reduced visibility is still large enough to observe the interference pattern. The same reasoning is expected to hold for the idler visibilities. This argument makes it possible to distinguish this scenario from the one where the visibility is positive and motivates further calculations of the signal and idler visibilities as a function of losses and increasing TWPA gain. These numerical calculations carried out by the Python program are described in the next section.

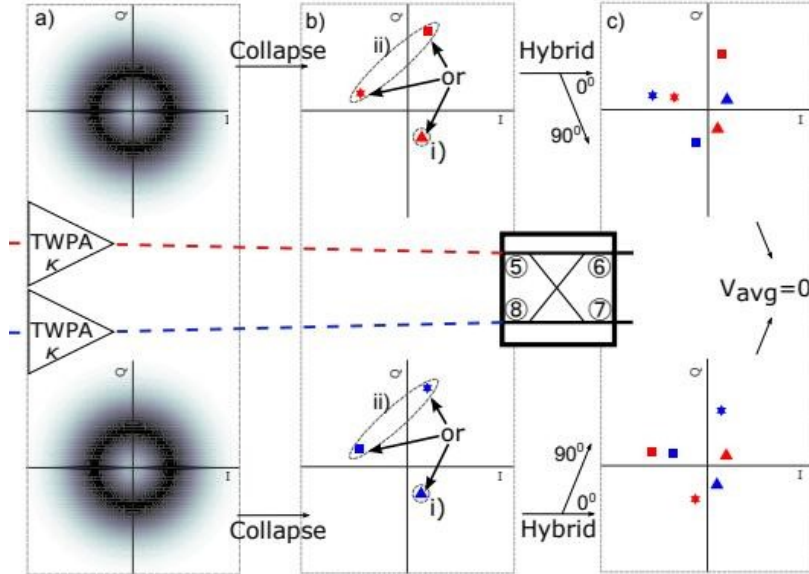


Figure 2.3. Expected scenarios regarding state collapse. The second part of the set-up depicted in fig. 2.1 is shown. (a) The bright centers within the two Wigner quasi-probability distributions (circles) indicate the undetermined phase of the states. In case of a collapse event, the states can collapse into the same state (b, case (i), triangles in both arms). A phase shift of  $90^\circ$  in one hybrid and transmission ( $0^\circ$ ) in the other one then results in  $V_{\text{stat}} = 0$  (c, upper and lower triangles with different colors) according to eq. (2.11).

Averaging over multiple events twins (stars) then still gives  $V_{\text{avg}} = 0$  (c, upper and lower stars and squares with different colors). Thus in case of a collapse event, as soon as collapse event start to play a roll, it will deviate from the expectation in fig. 2.3 and go down. The same reasoning is expected to hold for the idler visibilities.

## 2.2 Overview of the computer program

We use the two different solvers of the QuTiP module [12][13], a quantum computation toolbox in Python, to numerically evaluate the time evolution of the wave function (eq. (2.4)) with a Hamiltonian in the interaction picture that consists of the Hamiltonians of equations (2.6), (2.7) and (2.9). These are the Master Equation (ME) solver and the Monte Carlo solver (MC), of which the utilization in our calculations is described in subsections 2.2.1 and 2.2.2 respectively. In these subsections, we give a short description of how the aforementioned visibilities of the interference pattern are calculated using these solvers and treat both the case where insertion losses are neglected and the case where the effect of the power dissipation in the TWPA on the interference pattern is included. Before doing this, we give a short overview of the two parameters that are used by both solvers.

The dimensions of the signal and idler Hilbert space, the space of wave functions, are denoted as  $N_s$  and  $N_i$  respectively and referred to as  $N = N_s = N_i$ . Regarding the limitations of the program (which are mainly the available resources), only a truncated Hilbert space can be created. The truncation error that results from these finite dimensions is calculated in eq. (2.18) in section 2.2.1.

The amplification parameter  $\kappa$ , corresponding to the gain of a TWPA (eq. (2.13)), can be set as loop variable to investigate the magnitude of the interference visibility for an increasing TWPA gain. A larger photon number  $n$  in each of the arms with an amplifier requires a higher dimension of the Hilbert space  $N$ . Therefore,  $\kappa$  is limited by the aforementioned truncation error. Its maximum values for which the visibilities can be calculated with a maximum truncation error of 0.10% are plotted as a function of  $N$  in fig. C1 (Appendix C).

### 2.2.1 Master equation solver

For a given Hamiltonian, the function *qutip.mesolve* calculates the unitary (non-dissipative) timeevolution of a state vector  $|\psi\rangle$ . Using an ODE solver, it also evaluates the expectation values for the expect and collapse operator using the partial Hamiltonians in eqs. (2.6) – (2.9), at the times listed in the variable *t\_list*. By evaluating the points in time in this list, the correct coefficients as calculated by the functions for the partial Hamiltonians are passed on to the total Hamiltonian. After the output states have been calculated, the conditional photon distribution is computed. This in turn enables the program to calculate the expectation value of the signal and idler photons in detectors A and B. Finally, both the signal and idler average and statistical visibility of the interference pattern are calculated using these photon numbers and eq. (2.10) and eq. (2.11).

As doing ODE evolution requires multiple copies of the state vectors (or density matrices in the next case) in dense form, the required amount of RAM is significant and an important reason to run the calculations on a computational infrastructures with enough resources available. Because of the two arms of the interferometer with both signal and idler photons, the RAM usage is expected to scale with  $N^4$ . For density matrices, the same argument holds, except for the fact that these have dimensions  $N \times N$  instead of  $N$ . The RAM usage for calculations with these objects then is expected to scale with  $(N^2)^4 = N^8$ .

In the case where the effect of dissipation on the visibility is included, three different main elements appear in the calculations. First of all, density matrices instead of ket vectors are used. Secondly, jump operators<sup>1</sup> are initialized to account for the possibility of wave function collapse after interaction with a measurement apparatus. Thirdly, the time evolution of the density matrix  $\rho$  is expressed by the Lindblad formalism [14]:

$$\frac{d\rho}{dt} = -\frac{i}{\hbar}[\hat{H}, \rho] + \sum_{n=1}^{N^2-1} h_n (\hat{L}_n \rho \hat{L}_n^\dagger - \frac{1}{2} \{ \rho, \hat{L}_n^\dagger \hat{L}_n \}), \quad (2.14)$$

where  $\hat{J}_n = \sqrt{h_n} \hat{L}_n$  are the jump operators. Specifically, photons leaving the system and entering a thermal bath and vice versa are described by

$$\hat{J}_{out,n} = \sqrt{\Gamma(1 + n_{th})} \hat{a}_n \quad (2.15)$$

and

$$\hat{J}_{in,n} = \sqrt{\Gamma n_{th}} \hat{a}_n^\dagger \quad (2.16)$$

respectively, where  $\Gamma$  is the dissipation rate and

$$n_{th} = \frac{1}{\exp\left(\frac{\hbar\omega}{k_b T}\right) - 1}$$

is the thermal occupation number of photons in the bath. In all calculations, we set  $\omega_{s,i} = 2\pi \times 5$  GHz and  $T_{set-up} = 50$  mK, resulting in  $n_{th} = 8.3 \times 10^{-3}$ .

The insertion loss (IL) of the components is determined by the product  $\Gamma\Delta t$ , where we take  $\Gamma = 0.1$  for the whole set-up and where  $\Delta t$  represents the time that a photon state spends in a particular component shown in fig. 2.1, with corresponding Hamiltonians described in the time domain by eqs. (2.6) – (2.9). The insertion loss for the hybrids is known, which is why we keep this parameter fixed ( $\Delta t_h = 1$ ). For the TWPA, however, the insertion loss is unknown. To examine its effect on the signal and idler visibility, we vary  $\Delta t_{TWPA}$ , the time that a photon state spends in the TWPA.

---

<sup>1</sup> To avoid confusion with state collapse, the transition from a photon to the heat bath and vice versa is referred to as a jump, and therefore described by a jump operator in this context.

$$IL_{TWPA} (dB) = -10^{10} \log\left(\frac{P_{out}}{P_{in}}\right) = 10 \Gamma \Delta t_{TWPA}^{10} \log e \cong 4 \Gamma \Delta t_{TWPA} \quad (2.17)$$

As such, looping over  $\Delta t_{TWPA}$  in the computer program while keeping  $\Delta t = 1$  for the other components allows for a convenient way to vary the total dissipation in the TWPAs, calculate its effect on the magnitude of the interference visibilities and investigate if it has a limiting value for which the interference pattern cannot be observed. Recently fabricated TWPAs are reported to have an insertion loss of 4 dB at 10 GHz [15].

We define the truncation error (TE) as the relative error of the idler visibility that is calculated by using the ME solver (for example  $V_{i,ME} = 0.3330$ ) compared to the exact values of the idler visibility of  $1/3$ :

$$TE = \frac{V_{i,exact} - V_{i,ME}}{V_{i,exact}} = \frac{\frac{1}{3} - 0.3330}{\frac{1}{3}} \times 100 \% = 0.10 \% \quad (2.18)$$

This definition allows for using a criterion based on which the calculated visibilities can be rejected if the truncation error is larger than 0.10%, an error margin which is chosen for practical reasons. If this is the case, the idler visibility has a value below 0.3330 and the signal visibility is rejected as well.

### 2.2.2 Monte Carlo solver

To avoid the memory problem of the ME solver, we have investigated and used the Monte Carlo (MC) solver as an alternative [12][13]. The MC solver considers individual paths rather than the full time evolution. Continuously monitoring the environment of the quantum system, dissipation is always included in the calculations (originating from quantum jumps that occur randomly during the time evolution of the system) and information about the state of the system is increased [16][17]. The initial state must be a ket vector instead of a density matrix, but apart from this nearly all input arguments are taken the same as the ME solver. Regarding the steep increase of the RAM usage with  $N$  (which is expected to follow an  $N^8$  dependence due to the density matrices, as discussed in the previous section), this is definitely an advantage of using the MC solver for large quantum systems as ours. In this case the RAM usage is expected to scale with  $N^4$ , as only the state vector is required to be kept in the computer's memory.

The only new parameter is  $n_{traj}$ , the number of stochastic trajectories to be simulated, on which the accuracy of the result depends. Simulating the individual realizations of the system dynamics instead of describing the ensemble average over many identical realizations as done by the density matrix formalism introduces the so-called Monte Carlo error, defined as the standard deviation of the Monte Carlo estimator [18]:

$$MCE \equiv \sigma_{MC} = \frac{\sigma_{\phi}}{\sqrt{n_{traj}}}, \quad (2.19)$$

where  $\sigma_{\phi}$  denotes the standard deviation of some target quantity  $\phi$ .

Denoting  $\mathbf{X} = [X_1, X_2, \dots, X_{n_{runs}}]$  as a sample of  $n_{runs}$  replicates, then by the strong law of large numbers,  $\hat{\phi}_{n_{runs}} \rightarrow E[\phi(\mathbf{X})] = \phi$ , as  $n_{runs} \rightarrow \infty$ . As the total amount of simulated trajectories increases linearly with the amount of runs of the MC solver for a fixed number of paths,  $\sigma_{MC}$  is also expected to decrease as  $\frac{1}{\sqrt{n_{runs}}}$ . In line 6 in table B2 (Appendix B), the batch command that enables a user of the Maris cluster to run an example program multiple times (in this case 200) with the exact same parameters by submitting a job array is shown.

## 2.3 Heat-loss compensated calorimeter

In the final part of this chapter, we describe the heat transfer in the heat-loss compensated calorimeter regarding the processes which are expected to be present in our experiments. The insertion loss mentioned in the previous section, parameterized by  $\Gamma\Delta t_{TWPA}$  in eq. (2.17) and reducing the interference visibility, can be measured using this cryogenic calorimeter. A high power resolution of the calorimeter therefore enables us to make accurate predictions of the expected visibilities in the proposed interferometric experiment. After some of the concepts of heat transfer and calorimetry are introduced in the first subsection, a mathematical description of our thermal model is presented (2.3.2) and a preview of the calculation of the measured quantities is given (2.3.3).

### 2.3.1 Heat transfer and calorimetry

Given the three types of heat transfer (thermal conduction, thermal radiation and convection), we focus on the first one. The negligible role of convection is mentioned in the following discussion of the thermal properties relevant to our experiment, while in section 2.3.2. it is argued why we can neglect the contribution of thermal radiation.

The heat capacity  $C$  is a measure of how much heat  $Q$  an object can store,

$$C_p = \left( \frac{dQ}{dT} \right)_p, \quad (2.20)$$

where we define  $C_p$  (J/K) to be the lumped thermal capacitance of a solid for which the pressure  $p$  is kept constant. In this model the assumption is made that the temperature of the solid is spatially uniform at any moment during the transfer of heat, resulting in rapid conduction [19]. It is the most convenient method that can be used to solve transient heating and cooling problems. As a suitable criterion for substantiating the assumption of lumped system analysis to be applicable, we consider the Biot number ( $Bi$ ). This is the ratio between the resistance to thermal conduction and that of convective heat transfer (or in other words, the ratio of the heat transfer resistances *inside of* and *at the surface of* a body),

$$Bi = \frac{R_{cond}}{R_{conv}} = \frac{\left( \frac{L}{kA} \right)}{\left( \frac{1}{hA} \right)} = \frac{hL}{k}, \quad (2.21)$$

where  $L$  is the characteristic length of the object (m),  $k$  the thermal conductivity of the material (W/K) through which the heat is transferred,  $A$  is the area (m<sup>2</sup>) of the interface between the body and the helium gas the inner vacuum chamber of the cryostat (IVC), and  $h$  is the (convective) heat transfer coefficient  $q/\Delta T$  (W/(m<sup>2</sup>K)) (not to be confused with Planck's constant). The general view is that the error associated with the lumped capacitance method is small if  $Bi < 0.1$ . Since  $p_{IVC}$  is typically kept at a value of  $5 \times 10^{-4}$  mbar, we can regard the role of convective heat transfer as negligible, allowing for the application of lumped system analysis.

Anticipating on the experiment in which the thermal time constants of the components of the calorimeter will be determined by measuring their temperature as a function of time, we give a description of Newton's law of cooling, which is expected to be accurate in this case. This law states that the rate of heat loss per unit area for an object with a temperature  $T$  is proportional to the temperature difference between the object and its surroundings,

$$\frac{1}{A} \frac{dQ}{dt} = h(T - T_a), \quad (2.22)$$

where this time  $A$  is the heat transfer surface area (m<sup>2</sup>),  $Q$  is the thermal energy (J), and  $T_a$  is the ambient temperature [20]. Since the heat transfer coefficient is temperature-dependent, the regime of validity of this model is given by  $T - T_a \ll T$ , i.e. is it not valid for large difference between a body and its surroundings. This is not a strict and limiting criterion in our experiments, as is shown in chapter 3.

Given the definition of the heat capacity,  $C = \Delta Q / \Delta T$ , we can rewrite eq. 2.22 in terms of the time-dependent temperature,

$$\frac{dT}{dt} = -r(T - T_a), \quad (2.23)$$

where  $r = \frac{hA}{c}$  is a positive constant in units of inverse time.

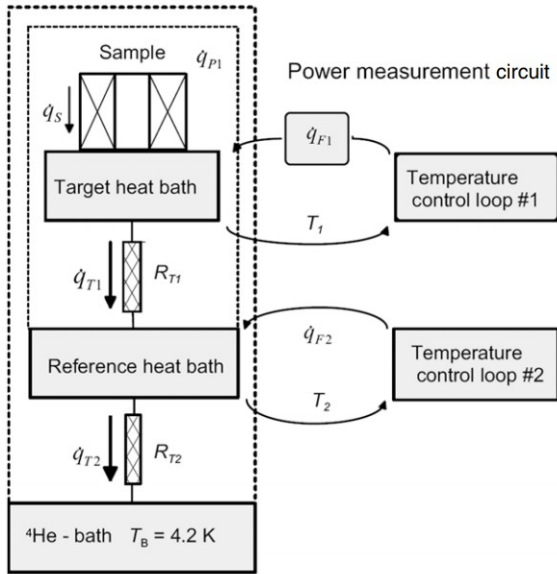
Its solution<sup>2</sup>,

$$T(t) = T_a + (T(0) - T_a)e^{-t/\tau}, \quad (2.24)$$

describes the exponential decay of the temperature difference to the ambient temperature for an object with initial temperature  $T(0)$ , with thermal time constant  $\tau \equiv \frac{1}{r} = \frac{c}{hA}$ . In literature [19][21], the value of the latter quantity is given as  $\tau = RC$ , with  $R_{th}$  being the thermal resistance (K/W):

$$R_{th} = \frac{L}{kA}. \quad (2.25)$$

Throughout the calculations for the quantities describing the heat transfer, we assume all values of the heat capacity and thermal resistance to be constant over the temperature range of our measurements. The validity of these approximations is considered in section 3.2. In the next section (2.3.2), this description of heat transfer will be used to calculate the thermal time constants for each of the components in our set-up in a different manner to check for the applicability of the solutions of Newton's law of cooling.



The importance of these time constants lies in the working principle of the calorimeter (fig. 2.4). The dissipated power of a sample can be calculated by keeping constant set temperatures and measuring the difference in the feedback power in the case of an applied power to the sample and in the case of no applied power. [22][23]. In order to make the two feedback systems effectively independent, the heat flow from the reference heat bath to the <sup>4</sup>He bath needs to be smaller than that from the target heat bath to the reference heat bath (i.e.  $\dot{q}_{T2} \ll \dot{q}_{T1}$ ), which can be realized by having  $R_{T2} \ll R_{T1}$  for the heat links between the components. This results in thermal time constants  $\tau_{ref} < \tau_{target}$ .

Figure 2.4. Schematics of a cryogenic dual compensated calorimeter, representing the (similar) set-up of an experiment conducted by Kajastie et al. The target and the reference bath are located inside a vacuum can. Constant set temperatures and feedback power allow for determining the dissipated power of a sample. Figure taken from [22].

<sup>2</sup> For  $T_a > T(0)$ , Newton's law becomes a law of heating, describing heat transfer in the reverse direction, with the same (higher) equilibrium temperature  $T_a$ .

A schematic overview is given in fig. 2.5, showing how the measurable variables and the components in the calorimeter are modeled for this experimental set-up (which is shown in fig. 3.1 in chapter 3). It is drawn in a way similar to fig. x in the next section (2.3.2) to allow the reader to verify the answers that follow from the calculations.

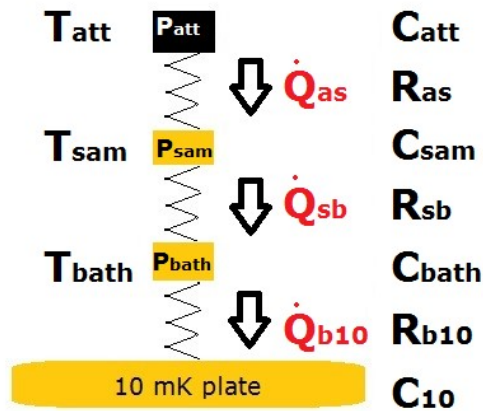


Figure 2.5. Schematic overview of the calorimeter. The heat capacities and thermal resistances of the components of the calorimeter are denoted as  $C$  and  $R$  respectively. The heat flow, measured temperatures and applied powers are denoted as  $\dot{Q}$ ,  $T$  and  $P$  respectively. The applied power to the heat bath,  $P_{bath}$ , is denoted by  $P_{ref}$  in chapter 3, since the heater is attached to the reference plate, which is part of the heat bath. From top to bottom:  $C_{att}$  (3 dB attenuator),  $R_{as}$  (connection to sample plate),  $C_{sam}$  (sample plate with sample heater and thermometer),  $R_{sb}$  (stainless steel piles connected to the heat bath),  $C_{bath}$  (heat bath consisting of a Cu holder and a reference plate with reference heater and thermometer),  $R_{b10}$  (connection to the 10 mK plate) and  $C_{10}$  (the 10 mK plate).

### 2.3.2 From a thermal model to differential equations

In this section, we transform the thermal model of our system (fig. 2.5) into an analogous electrical one, derive the corresponding differential equations for the heat flow and present the expressions for the quantities of interest.

We start with the notion that although there are physical differences between heat flow and current flow [24], the differential equations describing the flow are analogous. Writing the heat flow equation in a form similar to Ohm's law,

$$\Delta T = QR_{th}, \quad (2.26)$$

it can be seen that we can draw temperatures as voltage sources, depict the heat flow as a current flow and replace thermal resistances by electrical resistances [25][26]. Equivalently, heat capacitances can be drawn as electrical capacitances.

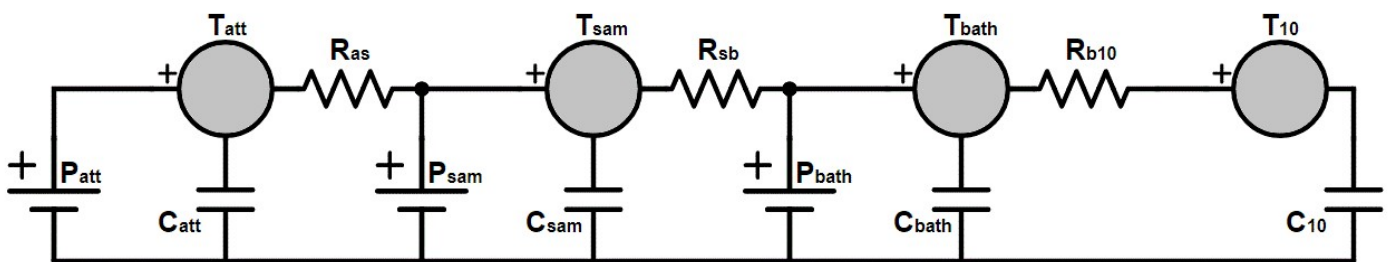


Figure 2.6. Electrical analogical scheme of heat transfer within the calorimeter that is attached to the 10 mK plate of the cryostat. The electrical components equivalent to the temperature, thermal resistance and heat capacitance within the experimental set-up are drawn. Using the law of conservation of energy around a closed circuit path, differential equations describing the heat flow within this system can be written down.

Using the law of conservation of energy around a close circuit path, an incoming heat flux can be stored and result in an outgoing heat flow at the same time. For the described components in our calorimeter, this results in the following coupled (thermal) differential equations of the system:

$$\text{Attenuator (att):} \quad P_{att} = \frac{T_{att} - T_{sam}}{R_{as}} + C_{att} \frac{dT_{att}}{dt} \quad (2.27)$$

$$\text{Sample plate (sam):} \quad P_{sam} + \frac{T_{att} - T_{sam}}{R_{as}} = \frac{T_{sam} - T_{bath}}{R_{sb}} + C_{sam} \frac{dT_{sam}}{dt} \quad (2.28)$$

$$\text{Heat bath (bath):} \quad P_{bath} + \frac{T_{sam} - T_{bath}}{R_{sb}} = \frac{T_{bath} - T_{10}}{R_{b10}} + C_{bath} \frac{dT_{bath}}{dt} \quad (2.29)$$

$$\text{10 mK plate (10):} \quad \dot{Q}_{Rad, 50 \text{ mK} \rightarrow 10 \text{ mK}} + \frac{T_{bath} - T_{10}}{R_{b10}} = \dot{Q}_{3He-4He} + C_{10} \frac{dT_{10}}{dt} \quad (2.30)$$

where T represents the temperature (K) of a component, P represents the dissipated power (W) at a component, R represents the thermal resistance (K/W) between the components: attenuator and sample plate ( $R_{as}$ ), sample plate and heat bath ( $R_{sb}$ ), and heat bath and 10 mK plate ( $R_{b10}$ ), C represents the heat capacity (J/K) of a component,  $\dot{Q}_{Rad, 50 \text{ mK} \rightarrow 10 \text{ mK}}$  represents the heat transfer rate due to thermal radiation from the 50 mK plate to the 10 mK plate and  $\dot{Q}_{3He-4He}$  represents the rate of the heat flow due to the cooling of the mixing chamber by the Helium flow.

We now justify why we can neglect the role of radiative heat transfer between the lowest two stages of the cryostat and the components of the calorimeter. The heat transfer between these copper plates is given by

$$\dot{Q}_{Rad, 50 \text{ mK} \rightarrow 10 \text{ mK}} = \frac{\sigma A (T_{50 \text{ mK}}^4 - T_{10 \text{ mK}}^4)}{\frac{1}{\epsilon_1} + \frac{1}{\epsilon_2} - 1} = 3 \times 10^{-15} \text{ W} \quad (2.31)$$

where  $\sigma$  represents the Stefan-Boltzmann constant ( $5.67 \times 10^{-8} \text{ W m}^{-2} \text{ K}^{-4}$ ), A represents the surface of the two parallel plates (we take  $A_1 = A_2 \approx 0.5 \text{ m}^2$ ) and  $\epsilon_1 = \epsilon_2 = 0.03$  is the emissivity of gold-plated copper. The assumption is made that all heat that is transferred from the surface of the 50 mK plate is intercepted by the surface of the 10 mK plate (i.e. the view factor, which is the proportion of the radiation that leaves one of the plates and strikes the other one, is taken equal to one and both the absorptivity as well as the reflectivity, which reduce the heat transfer, are not included in eq. (2.31).

As the surfaces of the components in the calorimeter are about one order of magnitude smaller, the temperature differences are comparable to those in our experiments and the minimum amount of dissipated power at a component is in the order of nanowatts, we can conclude that radiative heat transfer does not play a role of importance in our setup as well.

The 10 mK stage effectively acts as a heat sink, i.e. all heat that is dissipated in the calorimeter is eventually absorbed by the Helium flow. During our measurements, its temperature was constant, so we can take  $\frac{dT_{10}}{dt} \cong 0$  in eq. x.

We focus on the first three ordinary differential equations (ODEs), eqs. (2.27)-(2.29). Combining those gives the following third order ODE for  $T_{att}$ :

$$\begin{aligned} & [C_{bath} R_{sb} C_{sam} R_{as} C_{att}] \frac{d^3 T_{att}}{dt^3} + \left[ C_{bath} (R_{sb} C_{sam} + R_{sb} C_{att} + R_{as} C_{att}) + C_{sam} R_{as} C_{att} \left( \frac{R_{b10} + R_{sb}}{R_{b10}} \right) \right] \frac{d^2 T_{att}}{dt^2} + \\ & \left[ C_{bath} + C_{sam} + C_{att} + \frac{1}{R_{b10}} (R_{sb} C_{sam} + R_{sb} C_{att} + R_{as} C_{att}) \right] \frac{dT_{att}}{dt} + \frac{1}{R_{b10}} T_{att} - \left[ \frac{1}{R_{b10}} T_{10} + P_{bath} + \right. \\ & \left. \left( \frac{R_{b10} + R_{sb}}{R_{b10}} \right) P_{sam} + \left( \frac{R_{b10} + R_{sb} + R_{as}}{R_{b10}} \right) P_{att} \right] = 0 \end{aligned} \quad (2.32)$$

Before solving this, it is noteworthy to mention that the equilibrium temperature of the attenuator,  $T_{att}(\infty)$ , can easily be derived from this ODE. When this component is in thermal equilibrium, its first order time derivative equals zero, removing the higher order derivatives as well. We end up with the following expression:

$$\begin{aligned} T_{att}(\infty) &= T_{10} + R_{b10}P_{bath} + (R_{b10} + R_{sb})P_{sam} + (R_{b10} + R_{sb} + R_{as})P_{as} \\ &= T_{10} + \frac{P_{bath} + P_{sam} + P_{att}}{G_{b10}} + \frac{P_{sam} + P_{att}}{G_{sb}} + \frac{P_{att}}{G_{as}}, \end{aligned} \quad (2.33)$$

where the second expression is equivalent to the first one, but in terms of thermal conductance  $G = \frac{1}{R}$  between the stages. Similarly, for the sample plate and heat bath we have:

$$T_{sam}(\infty) = T_{10} + \frac{P_{bath} + P_{sam} + P_{att}}{G_{b10}} + \frac{P_{sam} + P_{att}}{G_{sb}} \quad (2.34)$$

$$T_{bath}(\infty) = T_{10} + \frac{P_{bath} + P_{sam} + P_{att}}{G_{b10}} \quad (2.35)$$

Returning to eq. (2.32). This is a third order ODE, in general not trivial to solve. We use Euler's Ansatz  $y(t) = y_0 e^{-rt}$  for solving the homogeneous linear differential equation of the m-th order with constant coefficients to arrive at the following characteristic equation:

$$Kr^3 - Lr^2 + Mr - N = 0, \quad (2.36)$$

where

$$K = C_{bath}R_{sb}C_{sam}R_{as}C_{att}, \quad L = C_{bath}(R_{sb}C_{sam} + R_{sb}C_{att} + R_{as}C_{att}) + C_{sam}R_{as}C_{att} \frac{R_{b10} + R_{sb}}{R_{b10}},$$

$$M = C_{bath} + C_{sam} + C_{att} + \frac{1}{R_{b10}}(R_{sb}C_{sam} + R_{sb}C_{att} + R_{as}C_{att}) \text{ and } N = \frac{1}{R_{b10}}$$

Rewriting eq. (2.36) gives

$$r^3 - lr^2 + mr - n = 0, \quad (2.37)$$

where

$$l \equiv \frac{L}{K} = \frac{G_{b10} + G_{sb}}{C_{bath}} + \frac{G_{sb} + G_{as}}{C_{sam}} + \frac{G_{as}}{C_{att}}, \quad m \equiv \frac{M}{K} = \frac{G_{b10}G_{sb} + G_{b10}G_{as} + G_{sb}G_{as}}{C_{bath}C_{sam}} + \frac{G_{b10}G_{as} + G_{sb}G_{as}}{C_{bath}C_{att}} + \frac{G_{sb}G_{as}}{C_{sam}C_{att}}$$

$$\text{and } n \equiv \frac{N}{K} = \frac{G_{b10}G_{sb}G_{as}}{C_{bath}C_{sam}C_{att}},$$

which is in agreement with the expression given by Domen et al. [27]. As the exact values of the coefficients are unknown, we consider the cases that one of the three temperatures is constant and proceed with finding the two remaining roots of this new characteristic equation. In fact, in the experiments this is achieved by PID control and the relaxation-time method (section 3.3). Therefore, in theory the reciprocal values of these roots should be equal to the two time constants.

Consider the case where the temperature of the heat bath is kept constant and  $P_{sam}$  and  $P_{att}$  are timeindependent as well. Rewriting eq. (2.32) for  $dT_{bath}/dt = 0$  then gives rise to the following second order ODE for  $T_{att}$ :

$$\begin{aligned} &\left[ C_{sam}R_{as}C_{att} \left( \frac{R_{b10} + R_{sb}}{R_{b10}} \right) \right] \frac{d^2 T_{att}}{dt^2} + \left[ C_{sam} + C_{att} + \frac{1}{R_{b10}}(R_{sb}C_{sam} + R_{sb}C_{att} + R_{as}C_{att}) \right] \frac{dT_{att}}{dt} \\ &+ \frac{1}{R_{b10}}T_{att} - \left[ \frac{1}{R_{b10}}T_{10} + P_{bath} + \left( \frac{R_{b10} + R_{sb}}{R_{b10}} \right)P_{sam} + \left( \frac{R_{b10} + R_{sb} + R_{as}}{R_{b10}} \right)P_{att} \right] = 0 \end{aligned} \quad (2.38)$$

Its characteristic equation has two roots and is as follows:

$$fr^2 - gr + h = 0, \quad (2.39)$$

where

$$f = C_{sam}R_{as}C_{att} \frac{R_{b10} + R_{sb}}{R_{b10}}, \quad g = C_{sam} + C_{att} + \frac{1}{R_1}(R_{sb}C_{sam} + R_{sb}C_{att} + R_{as}C_{att}) \quad \text{and} \quad h = \frac{1}{R_1}$$

Applying the quadratic formula, we find

$$r_{\pm} = \frac{g \pm \sqrt{g^2 - 4fh}}{2f} \leftrightarrow \tau_{\pm} = \frac{2f}{g \pm \sqrt{g^2 - 4fh}} \quad (2.40)$$

Now consider the case where the temperature of the sample plate,  $T_{sam}$ , is kept constant and  $P_{bath}$  and  $P_{att}$  are time-independent as well. Rewriting eq. (2.32) for  $dT_{sam}/dt = 0$  then gives rise to the following a second order ODE for  $T_{att}$  that is similar to eq. (2.38), with  $f$  and  $g$  are replaced by  $f'$  and  $g'$  respectively, where

$$f' = C_1(R_{sb}C_{att} + R_3C_{att}) + C_2R_3C_{att} \frac{R_1 + R_{sb}}{R_1} \quad \text{and} \quad g' = C_1 + C_2 + C_{att} + \frac{1}{R_1}(R_{sb}C_2 + R_{sb}C_{att} + R_3C_{att}),$$

with roots given by eq. (2.39) with  $f$  and  $g$  replaced by  $f'$  and  $g'$  respectively.

For a complete description of the temperatures as a function of time in terms of all thermal properties of the calorimeter, we refer again to the article by Domen et al. [27]. The general solution of the similar ODE describing the heat flow in a three-body calorimeter is given by

$$T_i(t) = \sum_{j=i}^3 \beta_{ij} e^{-r_j t} + T_i(\infty), \quad (2.41)$$

with coefficients  $\beta_{ij}$  for a fixed component  $i$  ( $i = 1, 2, 3$ ) that sum up to the temperature difference with the ambient,  $T(0) - T_i(\infty)$ , where  $T_i(\infty)$  describes the equilibrium temperature of component  $i$  (of which the expressions are strikingly similar to those given in eqs. (2.33) – (2.35)). The values of these coefficients for the components in our calorimeter are supposed to be given by a similar expression that follows from eqs. 15 - 22 in the article, but for practical reasons we do not derive these as well. Besides, an accurate estimate of these coefficients would require a very accurate estimate of the (temperature dependent) thermal properties, which is discussed in section 3.1.2.

In conclusion, Newton's law, as discussed in section 2.3.1 (eq. 2.24) and expected to be of importance in determining the thermal time constants, indeed follows from the differential equations that describe the heat flow through the components of the calorimeter (eqs. (2.27) – (2.29)). The solution of these ODEs is a sum of  $i$  exponentials, where  $i$  denotes the number of components with a non-constant temperature. Fitting this to cooling curve of a component then allows one to obtain the thermal time constants of the other time-dependent temperatures.

### 3 Experimental setup & Methods

In this chapter, the set-up is introduced in section 3.1. Details of the configuration used during the three runs that we performed are provided. Then, the material properties during the three runs are given and discussed in section 3.2, where calculations on the predicted thermal resistances, heat capacities and time constants are done as well. In the final section, section 3.3, an explanation about the measurement process and data acquisition is given.

#### 3.1 Cryogenic dual loss compensated calorimeter

The measurements on the calorimeter have been taken in a cryogenic environment, making use of 'The Little Snowman' at the Leiden University Institute of Physics (LION). This  $^3\text{He}$ - $^4\text{He}$  dilution refrigerator decreases the temperature of the lowest stage to 10-20 mK, enabling us to do our experiments at 30 mK and higher. The calorimeter is designed by Koen Bastiaans and fabricated by the Fine Mechanical Department at LION to investigate the power dissipation of a detection chip, achieving a power resolution of 100 nW at 4 K [28]. It has been attached to this copper plate to reach the same base temperature when no power is applied (fig. 3.1).

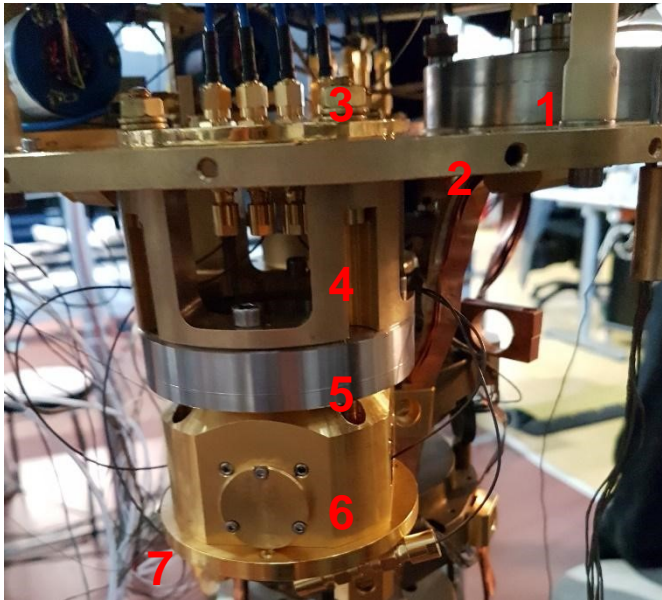


Figure 3.1. Picture of the calorimeter attached to the 10 mK plate, taken just before the third run (run 77). Some of the main components of the cryostat and calorimeter are indicated: the still (1), the 10 mK plate (2), a calibration line and a 3 dB attenuator (3), the brass base connecting the calorimeter to the 10 mK plate (4), the stainless steel cylinder (5), the Cu heat bath with the sample plate and 3 dB attenuator inside (6) and the reference plate (7).

Well-calibrated 4-point low-temperature thermometers are attached to the sample plate as well as the reference plate. Next to each of the thermometers an resistor (referred to as heater) is attached, resulting in an applied power for a given voltage (according to  $P = I^2 R$ ). For the sample plate, this is the MPR-20 22 ICJ with a temperature-independent resistance of  $220 \Omega$  and for the reference plate the RTO 20F  $47 \Omega$  5% W3 ( $R \approx 60 \Omega$  at  $T = 50$  mK) is used. Heaters with a higher resistance have been used during the third run, namely the MP930-1.00K-1% with a resistance of  $1 \text{ k}\Omega$  ( $R \approx 10 \text{ k}\Omega$  at  $T = 50$  mK). Details on the performance of both the thermometers and power are given in section 3.2.3.

### 3.2 Material properties and calculations on the three different experimental set-ups

The thermal conductivity and specific heat at temperatures as low as a few tens of millikelvins are investigated by Pobell [29]. The curves are given for a various amount of materials, including some of the ones present in our experiment: copper, alpha brass (65%Cu-35%Zn), aluminum and stainless steel (figs. 3.2 and 3.3). A characteristic feature in both graphs for almost all materials is the linear dependence of temperature in a log-log manner, the signature of a power law. Since most of the measurements of these properties have not been done at  $T = 30 - 80$  mK, we have used this feature to extrapolate the curves to find an estimate for their corresponding values. We are aware however, that this extrapolation is completely dependent from the assumption that the same power law holds in our range of temperatures. A possibly large error with respect to the other measured dimension of the components is introduced by extrapolation, but it still gives an estimate of the values that are required to do the calculations of the thermal properties shown later in this section.

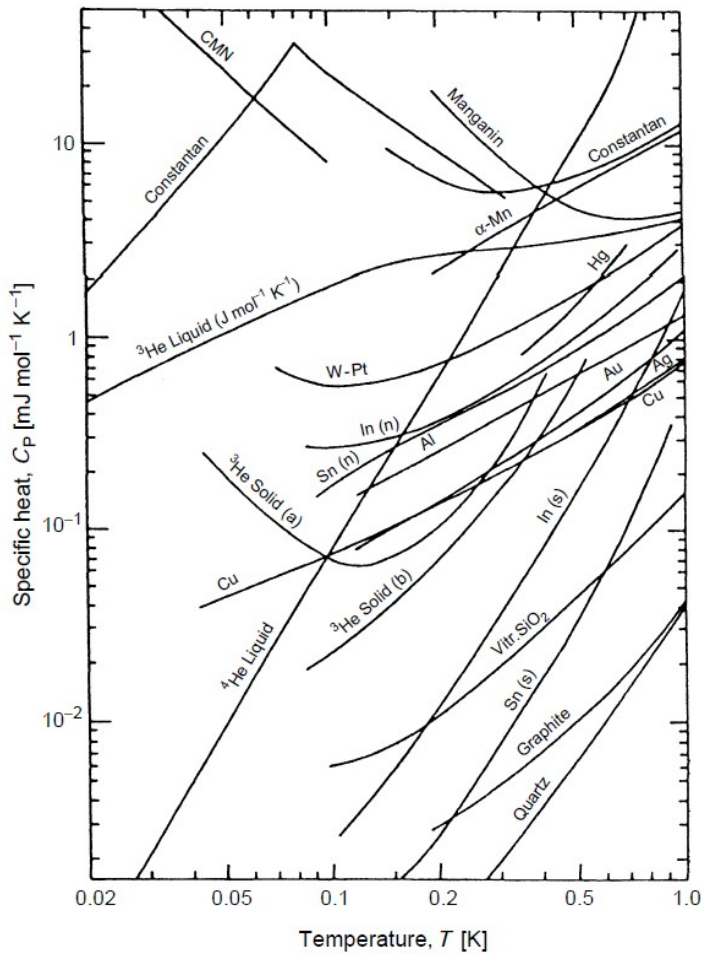


Figure 3.2. Typical specific heat capacities  $c$  of various materials below 1 K [29].

The specific heat capacity of stainless steel (SS) is not well-known in our temperature range, but with a similar power law dependence at low temperatures and a value of  $C_{SS} = 4 \times 10^{-1} \text{ Jkg}^{-1}\text{K}^{-1}$  at 1 K [30], we expect this property to have values between  $1 \times 10^{-2}$  and  $3 \times 10^{-2} \text{ Jkg}^{-1}\text{K}^{-1}$  for temperatures of 30 and 90 mK respectively. It is plausible that stainless steel has a higher specific heat capacity than both copper and brass, so we include its contribution to the specific heat capacity of component  $C_{\text{bath}}$  as displayed in fig. 2.5.

There are no values known for the specific heat capacity of brass in the temperature range of our measurements, yet there have been taken measurements at temperatures from 200 K down to 2 K for 65%Cu-35%Zn brass, where a value of  $C_{\text{brass}} = 3 \times 10^{-2} \text{ Jkg}^{-1}\text{K}^{-1}$  has been reported [31]. Regarding the fact that the heat capacity of copper is only slightly lower at the same temperature, while having a similar slope, we assume that the heat capacity of brass is comparable to that of copper.

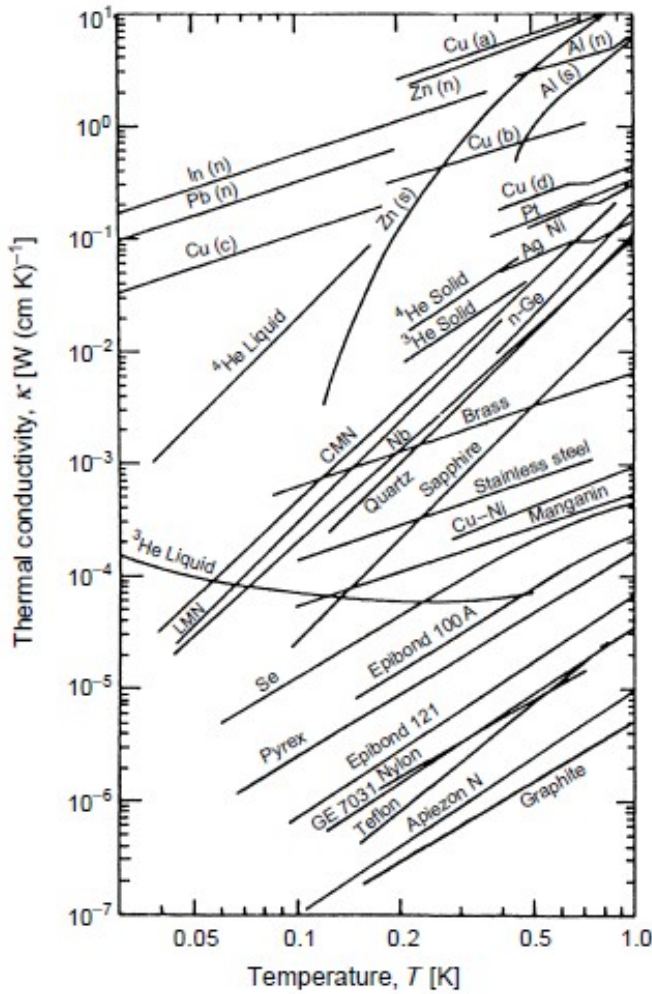


Figure 3.3. Typical thermal conductivities  $k$  of various materials below 1 K [29].

We summarize the extracted and extrapolated values from both graphs in SI units for a range of temperatures in table 3.1.

Thermal property	T=30 mK	T=40 mK	T=50 mK	T=60 mK	T=70 mK	T=80 mK	T=90 mK
$c_{Cu}$ (Jkg <sup>-1</sup> K <sup>-1</sup> )	$4.7 \cdot 10^{-4}$	$6.0 \cdot 10^{-4}$	$6.9 \cdot 10^{-4}$	$7.8 \cdot 10^{-4}$	$9.0 \cdot 10^{-4}$	$9.4 \cdot 10^{-4}$	$1.1 \cdot 10^{-3}$
$c_{SS}$ (Jkg <sup>-1</sup> K <sup>-1</sup> )							
$c_{Brass}$ (Jkg <sup>-1</sup> K <sup>-1</sup> )		$1.4 \cdot 10^{-3}$					
$c_{Al}$ (Jkg <sup>-1</sup> K <sup>-1</sup> )	$1.4 \cdot 10^{-3}$	$1.9 \cdot 10^{-3}$	$2.3 \cdot 10^{-3}$	$2.9 \cdot 10^{-3}$	$3.3 \cdot 10^{-3}$	$3.7 \cdot 10^{-3}$	$4.1 \cdot 10^{-3}$
$k_{Cu}$ (Wm <sup>-1</sup> K <sup>-1</sup> )							
$k_{SS}$ (Wm <sup>-1</sup> K <sup>-1</sup> )	$4.0 \cdot 10^{-3}$	$5.0 \cdot 10^{-3}$	$6.8 \cdot 10^{-3}$	$7.6 \cdot 10^{-3}$	$9.0 \cdot 10^{-3}$	$1.0 \cdot 10^{-2}$	$1.1 \cdot 10^{-2}$
$k_{Brass}$ (Wm <sup>-1</sup> K <sup>-1</sup> )	$1.2 \cdot 10^{-2}$	$2.3 \cdot 10^{-2}$	$2.9 \cdot 10^{-2}$	$3.8 \cdot 10^{-2}$	$4.2 \cdot 10^{-2}$	$4.9 \cdot 10^{-2}$	$5.4 \cdot 10^{-2}$
$k_{Al}$ (Wm <sup>-1</sup> K <sup>-1</sup> )							

Table 3.1. Temperature-dependent specific heat capacities and thermal conductivities for the materials used in our experiment.

The thermal conductivity of copper is several orders of magnitude higher than that of the other materials we used, which is why we neglect their contribution to the thermal resistance of the components as displayed in fig. 2.5.

We now provide the measured properties of the components for each of the three used set-ups and use these to calculate their thermal resistances and heat capacities of our thermal model in fig. 2.5. To this end, we use formula (2.25),  $C = cm$  (where the heat capacitance of an object equals its specific heat capacity times its mass) and  $\tau = RC$  and show the results in table 3.2. The material properties of the components during the first run (run 75) are used for the listed results to serve as an example for the calculated thermal properties in tables 3.3 and 3.4. Temperatures of 30 mK for the reference plate and 40 mK for the sample plate are used within these calculations, to reflect their typical temperature difference of 10 mK in the experiments. We do not take an integral over the different temperatures at the two sides of a thermal resistance, since the difference between the corresponding thermal conductivities is assumed to be smaller than the error resulting from reading and extrapolating the values in the graph. Instead, we choose to pick the value for the thermal conductivity at the highest temperature. We also mention any particularities and modifications with respect to the previous set-up.

Properties of system components	Value	Units
<i>Sample plate (40 mK)</i>		
Mass of the brass sample plate	$2.6 \cdot 10^{-3}$	kg
$C_{\text{brass}}$	$1.4 \cdot 10^3$	$\text{Jkg}^{-1}\text{K}^{-1}$
$C_{\text{sam}}$	$3.6 \cdot 10^{-5}$	$\text{JK}^{-1}$
$k_{\text{SS}}$	$5.0 \cdot 10^{-3}$	$\text{Wm}^{-1}\text{K}^{-1}$
$R_{\text{4\_SS\_piles}}$	$4.2 \cdot 10^5$	$\text{KW}^{-1}$
$R_{\text{4\_SS\_screws}}$	$2.0 \cdot 10^4$	$\text{KW}^{-1}$
$R_{\text{sb}} = R_{\text{piles}} + R_{\text{screws}}$	$10^5$ 4.4	$\text{KW}^{-1}$
$\tau_{\text{sam}} = R_{\text{sb}} C_{\text{sam}}$	$1.6 \cdot 10^1$	s
<i>Reference plate (30mK)</i>		
Mass of the Al (Au-coat) reference plate	$8.0 \cdot 10^{-2}$	kg
Specific heat capacity Al @ 30 mK	$1.4 \cdot 10^3$	$\text{Jkg}^{-1}\text{K}^{-1}$
$C_{\text{Al (Au-coat) reference plate}}$	$1.1 \cdot 10^{-4}$	$\text{JK}^{-1}$
Mass of the Cu holder	$7.3 \cdot 10^{-1}$	kg
Specific heat capacity Cu @ 30 mK	$4.7 \cdot 10^4$	$\text{Jkg}^{-1}\text{K}^{-1}$
$C_{\text{Cu holder}}$	$3.4 \cdot 10^4$	$\text{JK}^{-1}$
Mass of the SS cylinder	$6.7 \cdot 10^{-1}$	kg
Specific heat capacity SS @ 30 mK	$1 \cdot 10^2$	$\text{Jkg}^{-1}\text{K}^{-1}$
$C_{\text{SS cylinder}}$	$6.7 \cdot 10^3$	$\text{JK}^{-1}$
$C_{\text{bath}}$	$7.1 \cdot 10^3$	$\text{JK}^{-1}$
$k_{\text{SS @ 30 mK}}$	$4.0 \cdot 10^{-3}$	$\text{Wm}^{-1}\text{K}^{-1}$
$R_{\text{SS cylinder}}$	$1.5 \cdot 10^3$	$\text{KW}^{-1}$
$k_{\text{brass @ 30 mK}}$	$1.2 \cdot 10^2$	$\text{Wm}^{-1}\text{K}^{-1}$
$R_{\text{brass\_base}}$	$3.2 \cdot 10^3$	$\text{KW}^{-1}$
$R_{\text{b10}} = R_{\text{cylinder}} + R_{\text{base}}$	$4.8 \cdot 10^3$	$\text{KW}^{-1}$
$\tau_{\text{bath}} = R_{\text{b10}} C_{\text{bath}}$	$3.4 \cdot 10^1$	s

Table 3.2. Measured and calculated properties of the components in the calorimeter during the first run.

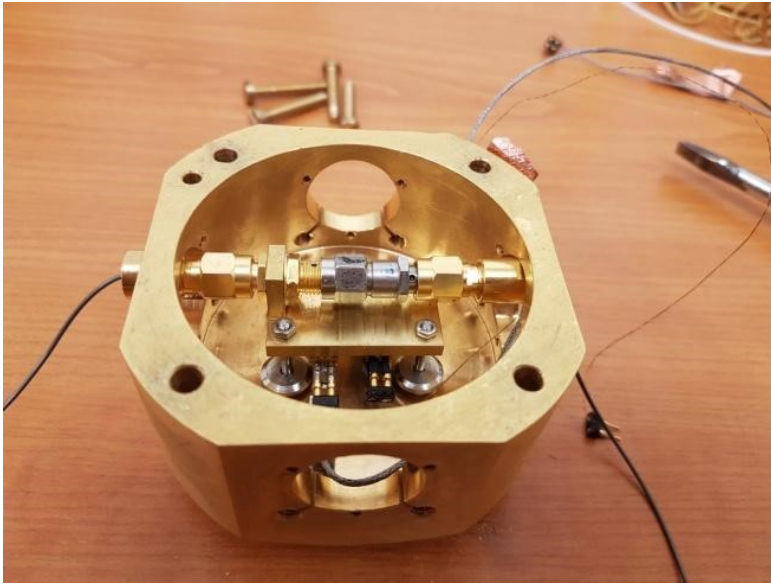
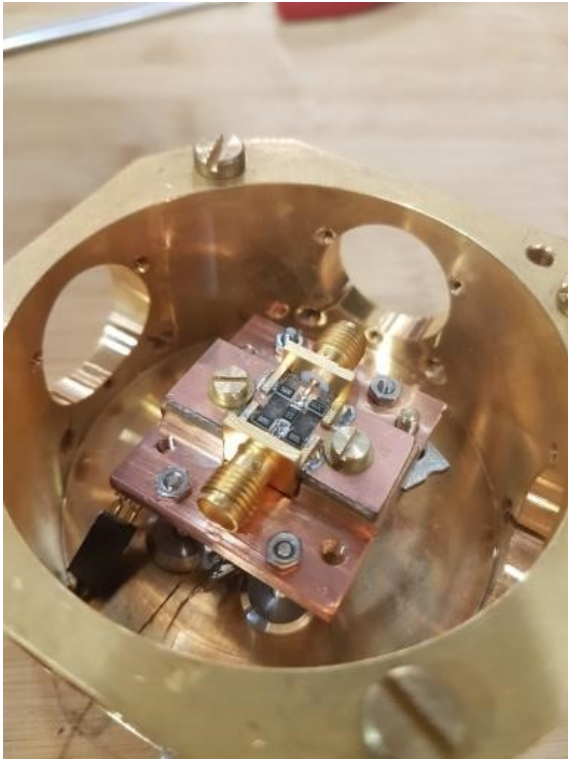


Figure 3.4. Picture of the 3 dB attenuator attached to a brass sample plate. The sample plate is connected to the Cu heat bath by four piles made of stainless steel.

In the first run (23/11/17 - 11/01/18), the 3 dB attenuator is connected to the brass sample plate by a brass rectangle (fig. 3.4). The 3 dB microwave pi attenuator consists of stainless steel connector bodies, goldplated beryllium copper center conductors, thin films on ceramic resistive circuits as resistors (with a total impedance of  $50 \Omega$ ) and PTFE (Teflon) insulators. Presumably, the specific heat capacity of PTFE is at the order of only a few micro joules between 40 and 90 mK [32]. In principle, this would result in a small value of the heat capacity of the attenuator.

Heat capacity (C) or thermal resistance (R)	Value
$C_{sam}$	$3.6 \cdot 10^{-5} \text{ J/K}$
$R_{sb}$	$4.4 \cdot 10^5 \text{ K/W}$
$\tau_{sam} = R_{sb} C_{sam}$	$1.6 \cdot 10^1 \text{ s}$
$C_{bath}$	$7.1 \cdot 10^{-3} \text{ J/K}$
$R_{b10}$	$4.8 \cdot 10^3 \text{ K/W}$
$\tau_{bath} = R_{b10} C_{bath}$	$3.4 \cdot 10^1 \text{ s}$

Table 3.3. Measured and calculated properties of the components in the calorimeter during the first run.



For the second run (01/03/18 - 12/03/18), a Cu sample plate with a better thermalization to the attenuator is used (fig 3.5). The latter was made in-house with the same goal. The mass of the copper sample plate is the same as the one made of brass. The specific heat capacity of the materials being comparable,  $C_2$  is probably smaller but is well-known this time. The heat flow through this new attenuator is discussed in section 4.3.1.

Figure 3.5. During this run, a new 3 dB attenuator is used designed to have a better thermalization. It is attached to a Cu sample plate.

Heat capacity (C) or thermal resistance (R)	Value
$C_{sam}$	$1.6 \cdot 10^{-5} \text{ J/K}$
$R_{sb}$	$4.4 \cdot 10^5 \text{ K/W}$
$\tau_{sam} = R_{sb} C_{sam}$	$7.3 \cdot 10^0 \text{ s}$
$C_{bath}$	$7.1 \cdot 10^{-3} \text{ J/K}$
$R_{b10}$	$4.8 \cdot 10^3 \text{ K/W}$
$\tau_{bath} = R_{b10} C_{bath}$	$3.4 \cdot 10^1 \text{ s}$

Table 3.4. Measured and calculated properties of the components in the calorimeter during the first run.

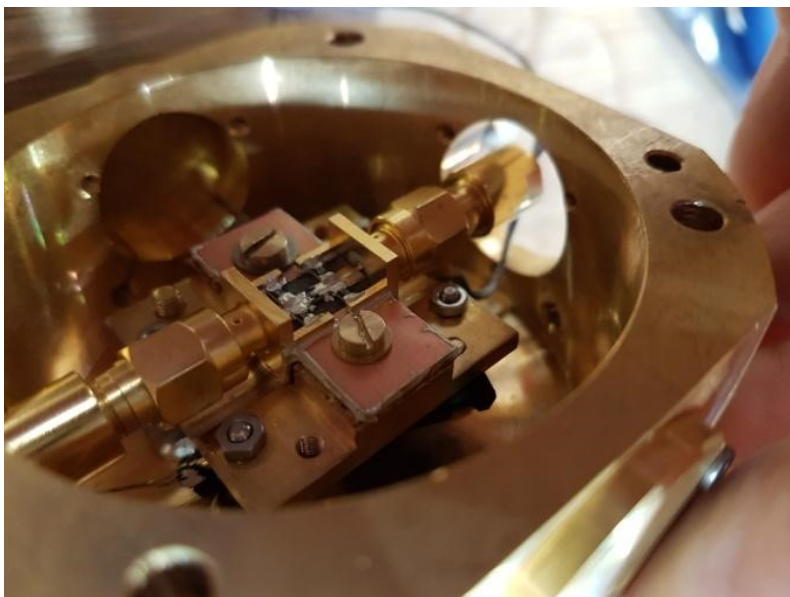


Figure 3.6. The same set-up as in the previous run is used, except that the reference plate attached to the heat bath is made of copper. Next to this, silver epoxy is applied to the attenuator, again with the goal of having a better thermalization.

Run 3 (22/03/18 - 29/03/18): A Cu reference plate is used instead of the Al(Au-coated) one. The same attenuator is used, but silver epoxy is applied this time, so its thermal resistance should be lower than in run 2.

Heat capacity (C) or thermal resistance (R)	Value
$C_{sam}$	$1.6 \cdot 10^{-5}$ J/K
$R_{sb}$	$4.4 \cdot 10^5$ K/W
$\tau_{sam} = R_{sb} C_{sam}$	$7.3 \cdot 10^0$ s
$C_{bath}$	$4.7 \cdot 10^{-4}$ J/K
$R_{b10}$	$4.8 \cdot 10^3$ K/W
$\tau_{bath} = R_{b10} C_{bath}$	$2.3 \cdot 10^0$ s

Table 3.5. Measured and calculated properties of the components in the calorimeter during the first run.

### 3.3 Methods

The data are acquired as follows. A cryogenic resistance bridge (AVS-46) uses a 4-wire measurement to determine the temperature-dependent resistance of a calibrated sensor (the low-temperature thermometer mentioned in section 3.1.1). Resistances of the thermistors and heaters are measured by a breakout box. The measuring current is kept at a minimum to maintain a good accuracy of the sensor, which is very sensitive to  $I^2R$  heating and therefore kept at a minimum of picowatts. The corresponding output voltages are read and recorded by a DAQ card (NI USB-6343 16-Bit, 500 kS/s), which is connected to a PC. A Python program named `Calorimeter.py` is written by Tom van der Reep to convert these by using the relationship between temperature and measured resistances. The temperatures of the sample plate and reference plate (which is part of the heat bath) can both be calculated from these resistances and displayed real-time. An example of the user interface of this program during the measurements is shown in fig. C11 (Appendix C).

We report typical values for the first run (Run 75), which was the most successful one due to reference temperature being at a minimum of 30 mK, about 10 mK above the temperature of the mixing chamber. Using a PID controller, we are able to keep the sample plate and reference plate at constant temperatures with standard deviations of 0.03 mK at 33.00 mK up to 0.15 mK at 80.00 mK. Tuning of the controller parameters is done manually and based on the Ziegler-Nichols rules [33], with values for the proportional gain  $K_p$  between  $10^{-12}$  and  $10^{-7}$ , integral gain  $K_i$  between  $10^{-14}$  and  $10^{-11}$ , and differential gain  $K_d$  between  $10^{-20}$  and  $10^{-15}$ . The heaters on the sample plate and reference plate, which are connected to the PC the same way as the thermometers, are programmed to adjust their power input according to these controller parameters in order to reach the set temperatures. The amount of applied power depends on the temperature difference between the sample plate and the reference plate, the temperature difference between the reference plate and the 10 mK plate, and on the temperature of each of the components of the calorimeter. Typical values of  $P_{\text{sam}}$  and  $P_{\text{ref}}$  that are applied to keep the sample and reference plate at their set temperatures are plotted as a function of the temperature difference between these components, showing a linear dependence (fig. C9, Appendix C).

The measurement procedure for determining the thermal time constants of the components in the calorimeter consists of the following steps. First of all, the set temperatures of the sample and reference plate are chosen in a range of 30 - 110 mK, with the sample temperature being higher than that of the heat bath. For most measurements, the initial temperature difference between the two plates is 10 mK, but cooling curves for larger differences up to 40 mK are also measured. Regarding eq. (2.41) in section 2.3.2 and the discussion of the temperature-dependent thermal properties of the component, it can be seen that the choice of the set temperatures affects the thermal time constants. Secondly, the PID constants are tuned (as described above). The applied powers of both heaters need to be constant to prevent additional heat flow from components with a non-constant temperature. Tuning parameters are adjusting until the observed margin of error of all measured temperatures and applied power are as small as possible. Thirdly, we apply the relaxation-time method as described in [21]. The PID controller for the temperature of the sample plate or the reference plate is turned off, resulting in a sudden drop of temperature and eventually to the equilibrium temperature of the reference plate or 10 mK plate respectively. As discussed in section 2.3.2, two remaining thermal time constants are expected to determine the slope of the cooling curve.

Finally, the output data, consisting of the measured temperatures for and applied powers to both the sample and reference plate, is saved as text file and processed in MATLAB. Using MATLAB's Curve Fitting Toolbox, eq. (2.41) is used as fitting equation, where we take the sum of two exponentials instead of three (since one of the temperatures is kept constant).

## 4 Results & Discussion

After the theoretical considerations about the calculations of the interference visibility and the heat transfer in our experimental set-up, in this chapter the experimental results are presented in the same order, alongside with a discussion of the obtained results. Section 4.1 starts with the resulting visibilities for the set-up as depicted in fig. 2.1. in the case that the effect of insertion losses on the visibilities is excluded. Then, in section 4.2, this effect is included in the calculations, both for those in which the Master equation (ME) solver is used and those in which is made use of the Monte Carlo (MC) simulations. The chapter ends with the results of the three experiments in which the thermal time constants of the attenuator, sample plate and heat bath are determined (section 4.3).

### 4.1 Calculations excluding losses

#### 4.1.1 ME solver

Following the description of the signal and idler visibility in section 2.1.2, we have calculated these quantities again using the ME solver in the computer program (section 2.2) and eqs. (2.10) and (2.11). Regarding the visibility criterion (eq. 2.18) and the available resources, we have used a dimension of the Hilbert space of  $N = 99$  to calculate the visibilities for 18 loop steps from  $\kappa = 0.0$  to  $\kappa = 1.7$ , corresponding to a TWPA gain up to 13.4 dB (fig. 4.1). As expected, for increasing  $\kappa$ , all curves come close to the exact value of  $1/3$  in the limit of large gain.

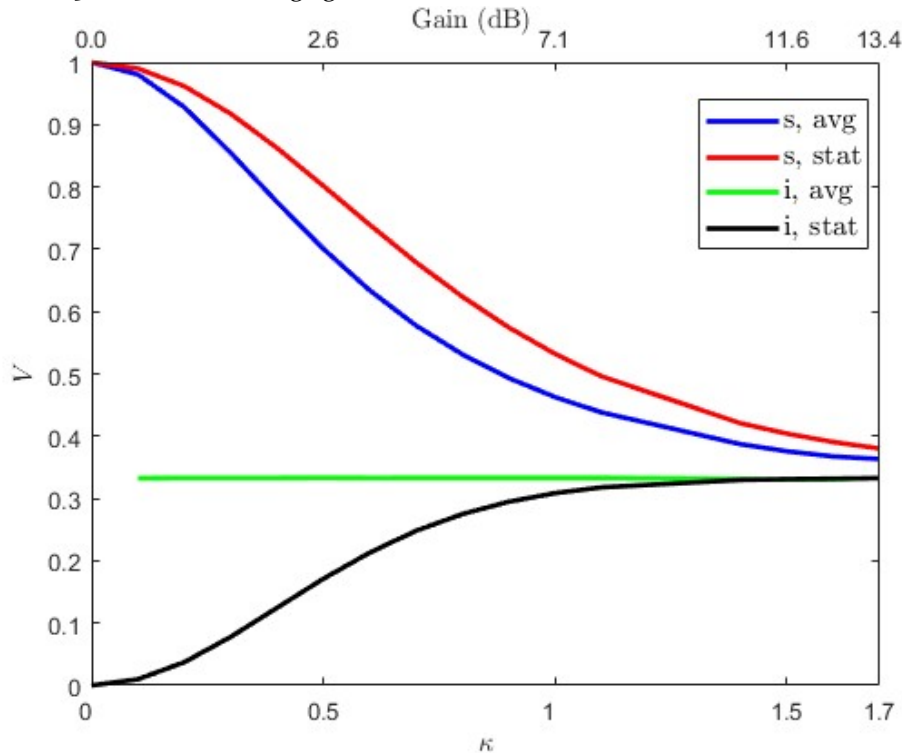


Figure 4.1. Expected signal and idler average and signal visibilities as a function of  $\kappa$  (corresponding with the gain of each of the TWPAs) according to the expression for the average and statistical values given by eqs. (2.10) and (2.11). In the limit of large gain, all curves come close to  $1/3$ . Comparing this graph to the previous calculations of the visibility (fig. 2.2), we see that the statistical idler visibility does not exceed the average idler visibility.

By using the *sacct* command in Slurm (line 6 in table B1, Appendix B), we have found the required amount of RAM and computation time for completed jobs. To show the vast amount of required resources, the RAM usage of the program with the ME solver is plotted as a function of  $N$  for the case where dissipation excluded and included in figures 4.2 and 4.3 respectively. They indeed follow an  $N^4$  dependence, as expected in section 2.2.1.

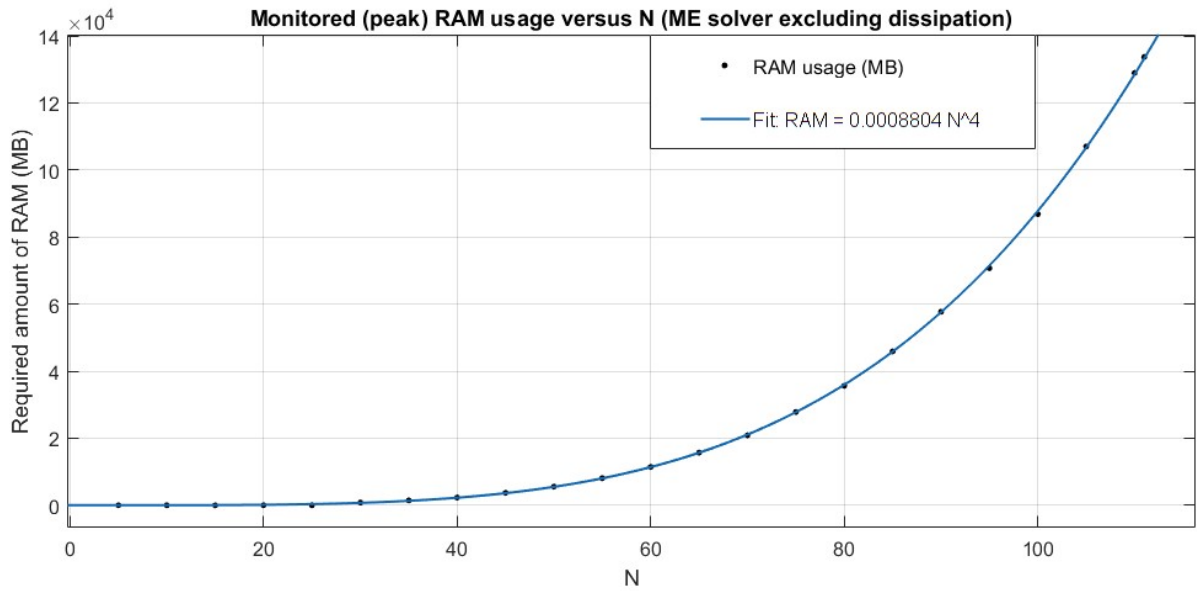


Figure 4.2. Monitored peak RAM usage as a function of the dimension of the Hilbert space  $N$ . As expected in section 2.2.1, the RAM usage scales with the fourth power of  $N$ .

After running the program with the memory profiler *mem\_profiler* for different  $N$ , it was confirmed that creating the operators and the Hamiltonians accounts for the majority of the RAM usage (e.g. 9.4% for creating the Hamiltonian for the first hybrid and 59.3% in total). The other part is required to store the coefficients that are calculated in the functions designated for this purpose. Regarding fig. 4.2, it is not clear at this point why the program crashes for  $N > 111$ , as the 500 GB of RAM on the used node should be sufficient. Table C1 (Appendix C) combines the results of this figure with the empirical formula of fig. C1 for one loop step to extrapolate for higher kappa.

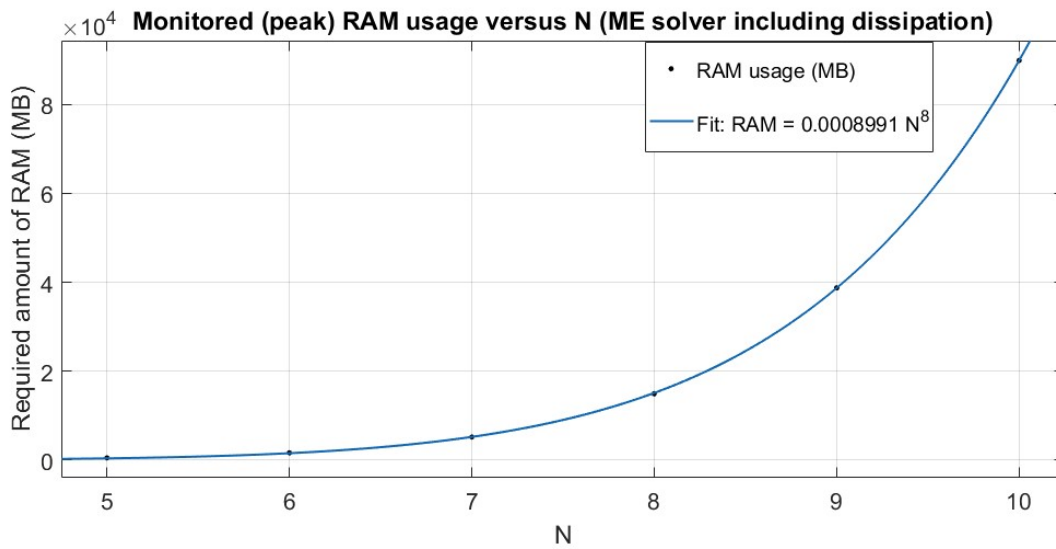


Figure 4.3. Monitored peak RAM usage as a function of the dimension of the Hilbert space  $N$ . As expected in section 2.2.1, the RAM usage scales with the eighth power of  $N$ .

The program crashes for  $N > 10$  for the same reason as stated in section 4.1.1. Since the required amount of RAM for the density matrices created here scales with  $(N^4)^2 = N^8$  instead of  $N^4$ , this means that the prediction made in section 2.2.1. made sense. To check whether the RAM usage is monitored correctly by SLURM, we have tested the program with the same parameters on a high memory node with 1.5 TB of RAM available (Appendix A). As shown in in table C1 in Appendix C, we expected to be able to run the program with a value of  $N$  that was sufficiently high to calculate the visibilities for  $\kappa = 2.0$  (or at least a higher  $\kappa$  than calculated on the Maris cluster). Instead, the program crashes again at  $N = 112$ . The received error is in both cases the same:

*TypeError: fast\_csr\_matrix allows only int32 indices.*

The error is raised, because QuTiP uses 32 bit indices. At the time that this module was written, this was all that SciPy supported. By explaining the issue on the GitHub forum to the developers of QuTiP along with other users who experienced similar problems, a discussion of how to solve this has been initiated. It is uncertain if using int64 for the compressed sparse matrix indices in QuTiP will be possible in the nearby future, but it is clear that the program itself contains no wrong code and that the QuTiP internals need to be modified in order to calculate the visibilities for higher amplifications.

## 4.2 Calculations including losses

When including the effect of dissipation on the interference visibility, this quantity is lower compared to the lossless case. Here we investigate if the reduced visibility is still large enough for high gain and a large insertion loss at a temperature of 50 mK, so that it can be distinguished from the case where the wave function has collapsed (resulting in a visibility of zero). We approximate the value of the insertion loss in dB by  $4\Gamma\Delta t_{TWP A}$  (eq. 2.17). First we show the results that follow from solving the master equation with density matrices, then the resulting visibilities calculated by taking the average value of the outputs from the Monte Carlo simulations are shown together with the results from the ME solver for comparison.

### 4.2.1 ME solver

Regarding the increased amount of required RAM compared to the lossless case due to the presence of density matrices and the aforementioned TypeError, a dimension of the Hilbert space of  $N = 10$  is used to calculate the average visibilities for 10 loop steps from  $\kappa = 0.0$  to  $\kappa = 0.6$  and insertion losses up to 6 dB (fig. 4.4). The idler visibilities seem to converge to a constant value in the limit of large gain, independent of the insertion loss. This is good news, since their magnitude was already quite low but remains sufficiently greater than zero, allowing the experimentalist to observe the interference pattern. For the signal visibilities, there is no conjecture about its magnitude for large gain at this point.

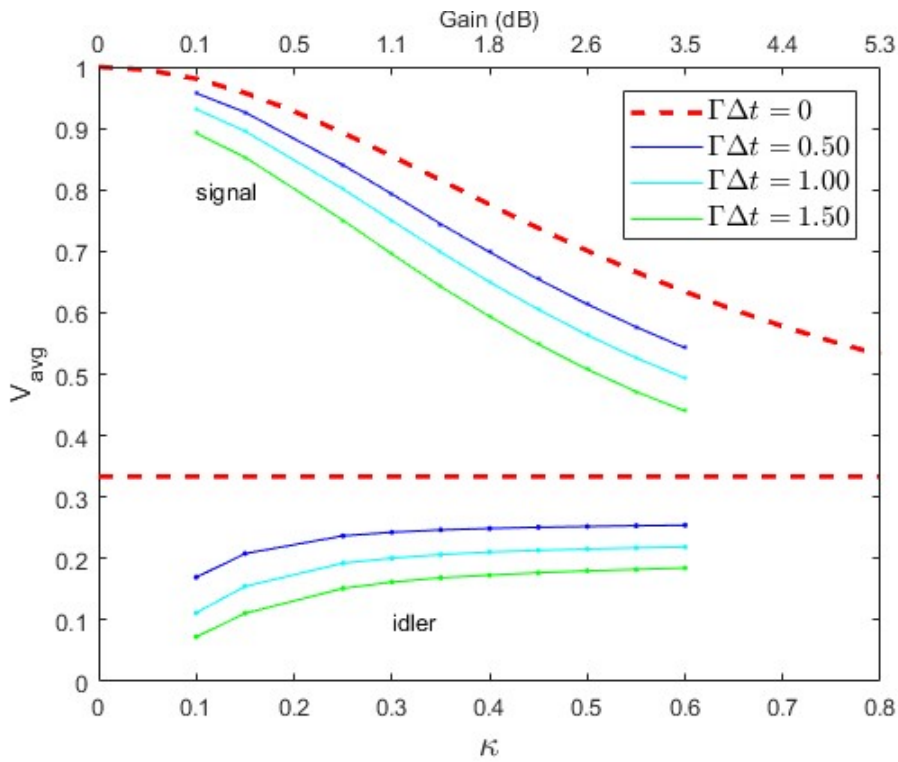


Figure 4.4. Expected reduced average signal and idler visibilities as result of heat dissipation of the TWPAs, plotted as a function of  $\kappa$  for an insertion loss of 2 dB (blue), 4 dB (light blue) and 6 dB (green). To give a clear view, the curves for the insertion losses in between are not shown. The reader is referred to figure C6 in Appendix C for these curves. The theoretical visibilities for the lossless case have been included as well as comparison.

In figure 4.5, the calculated values for the average visibilities in the lossless case have been subtracted from the ones in figure 4.4. In this way, it is easier to see to which extent they differ from each other and how this difference behaves for a large amplifications. As mentioned at the beginning of this section, the idler visibilities seem to converge to a constant value in the limit of large gain, which is expressed by the differences that converge to a constant value as well. It can be seen that the difference in the signal visibilities appear to also become constant, e.g. for  $\kappa = 0.6$  and an insertion loss of 6 dB, this is almost 0.2 lower than in the lossless case. If this is true, the magnitude of the signal visibilities remains also greater than and distinguishable from zero in the limit of large gain.

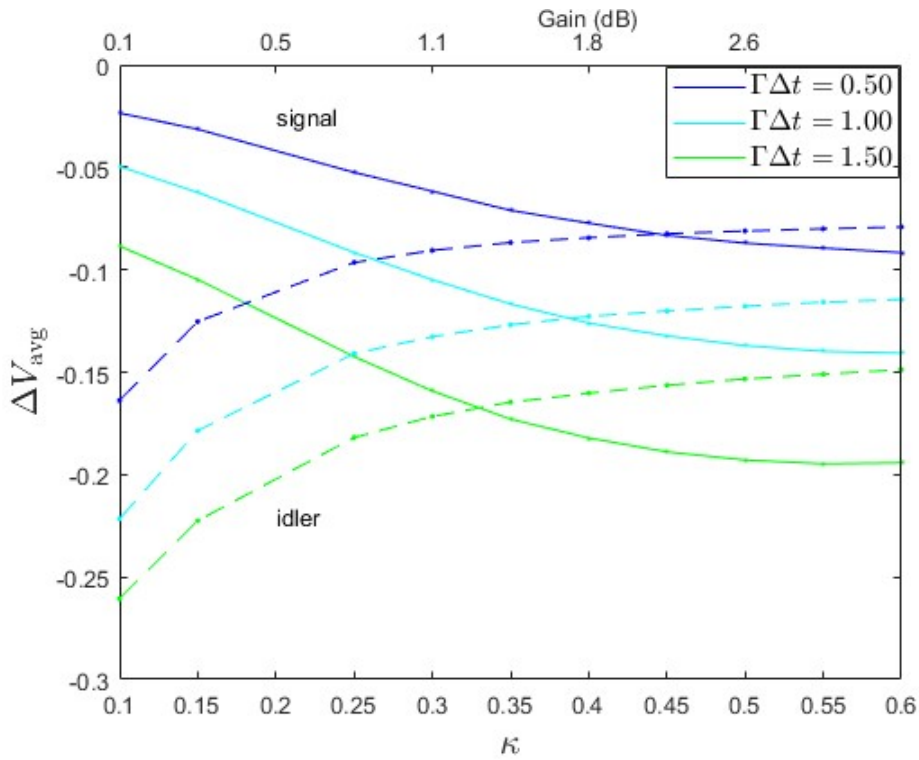


Figure 4.5. Difference plot of the average signal (solid lines) and (dotted lines) visibilities calculated by the ME solver, where  $\Delta V_{\text{avg}} = V_{\text{avg}} - V_{\text{exact}}$  as a function of  $\kappa$  for an insertion loss of 2 dB (blue), 4 dB (light blue) and 6 dB (green). To give a clear view, the curves for the insertion losses in between are not shown. All differences appear to converge to constant values.

#### 4.2.2 MC solver

We continue with the results obtained by running Monte Carlo simulations. In figure 4.6, the average signal visibility  $V_{\text{avg},s}$  is taken as target quantity and its histogram is plotted to show how the realizations of the MC solver with a fixed number of trajectories are distributed. Fitting a Gaussian to this histogram shows that the strong law of large number indeed seems to hold, with a mean signal visibility  $V_{s,MC} = 0.74658$  close to  $V_{s,ME} = 0.74689$ .

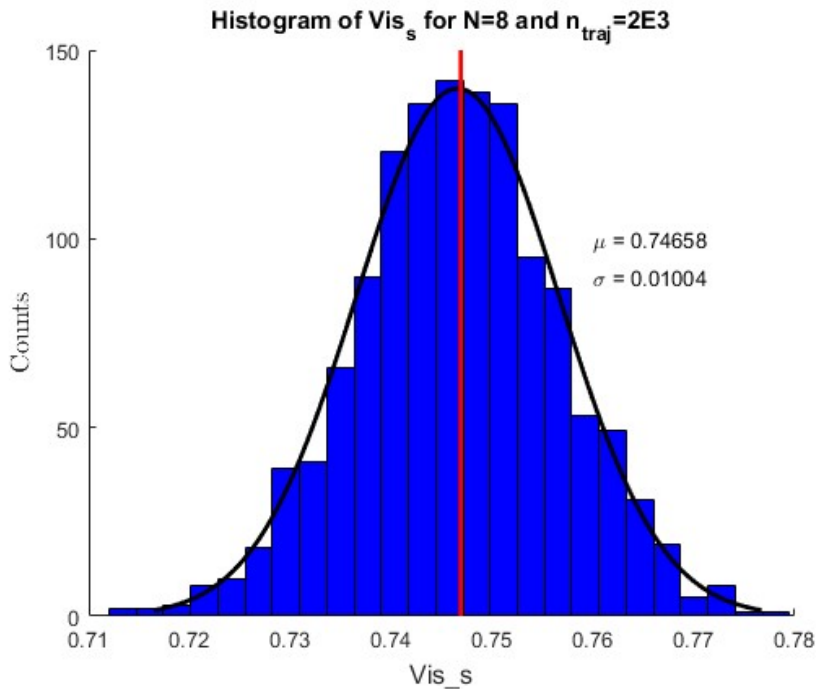


Figure 4.6. Distribution of the average signal visibilities ( $\text{Vis}_s$ ) calculated by using the Monte Carlo solver. The program has run this solver 1,304 times, each with  $N=8$  and 2,000 simulated stochastic trajectories used to calculate  $V_{s,MC}$  for  $\kappa = 0.3$  and  $\Delta t_{\text{TWPA}} = 10$ . A Gaussian fit (black) to this histogram shows that the visibilities that follow from the MC solver follow a normal distribution. The obtained mean value of this distribution is the resulting (signal) visibility, a relative error of only 0.04 % compared to the visibility calculated with the same parameters by the ME solver (indicated by the red line).

As shown above, the MC solver is an accurate way of obtaining the visibilities for the same Hamiltonian. As it concerns a statistical approach instead of an analytical solution, the visibilities are accompanied by error bars, calculated for  $\kappa = 0.1 - 0.8$  (fig. 4.7) and insertion losses up to 6 dB. In both this figure and figure 4.4., the analytical visibilities from the previous section, calculated by solving the master equation, are included for comparison. Furthermore, additional data points for  $\kappa = 0.0 - 0.2$  obtained by the ME solver are shown to complete the curves for a low gain.

All ME visibilities lay within the confidence intervals obtained from the MC solver and in most cases even in the exact middle, showing good agreement between the two approaches of calculating the interferences visibilities. Equally important, although by inductive reasoning, it gives a good reason to trust the outcomes for the visibilities calculated for  $\kappa = 0.7$  and  $\kappa = 0.8$ , which cannot be calculated and verified by the ME solver at this moment. Finally, we also note that we now have more evidence that points in the direction of constant visibilities in the case of large gain and power dissipation in the amplifiers. For the idler visibility this is evident, while for the signal visibility the plot that shows the deviation from the visibility in the lossless case (fig. 4.1) hints that this difference is constant in the limit of large gain.

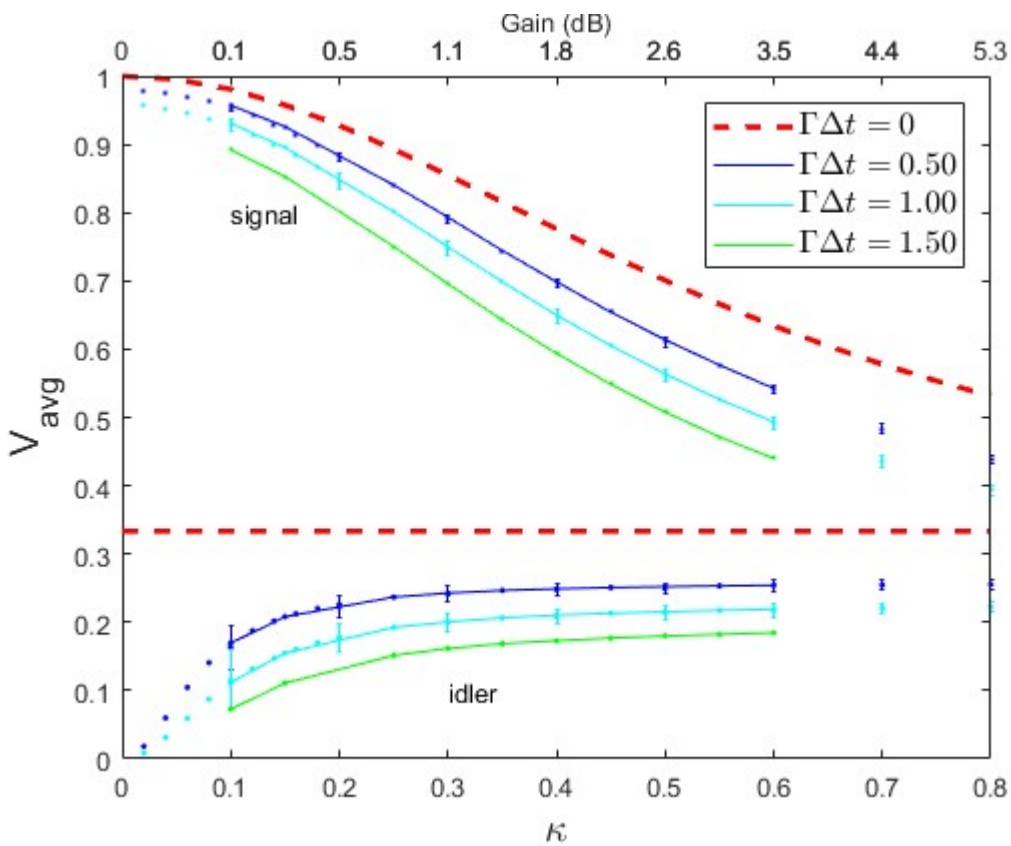


Figure 4.7. Expected reduced average signal and idler visibilities (shown with error bars) as result of heat dissipation of the TWPAs obtained from running Monte Carlo simulation and plotted as a function of  $\kappa$  for an insertion loss of 2.2 dB (blue), 4.3 dB (light blue) and 6.5 dB (green). The ME visibilities are shown as well, showing good agreement between the two approaches. To give a clear view, the curves for the insertion losses in between are not shown. The theoretical visibilities for the lossless case (red-dotted line) have been included as well as comparison, just like some additional points for  $\kappa = 0.0 - 0.2$  resulting from the ME solver (not fitted to the ME visibilities for  $\kappa = 0.1 - 0.6$ ).

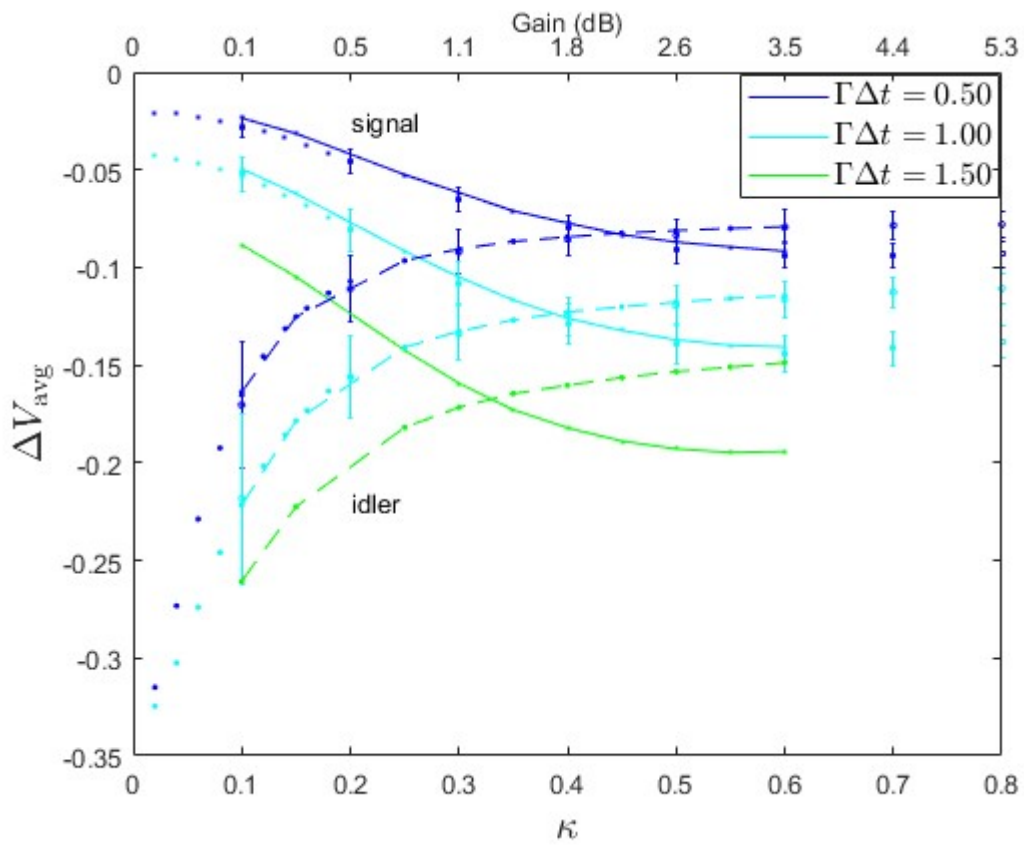


Figure 4.8. Difference plot of the average signal (solid lines) and idler (dotted lines) visibilities using the MC solver, where  $\Delta V_{\text{avg}} = V_{\text{avg}} - V_{\text{exact}}$  as a function of  $\kappa$  for an insertion loss of 2 dB (blue), 4 dB (light blue) and 6 dB (green). To give a clear view, the curves for the insertion losses in between are not shown. Even for this larger amplification, all differences appear to converge to constant values.

### 4.3 Thermal time constants

In this section, the measurements done on the time constants of the components within the calorimeter are presented in sections 4.3.1 for runs 75 until 77 respectively. While these measurements have been carried out for a various range of temperatures, we have chosen to show only a few of them. The focus lies on understanding the magnitudes of the time constants that follow from the exponential fits that follow from section 2.3.2, regarding the different configurations of the calorimeter (3.2.2).

#### 4.3.1 Run 75, 76 and 77

Figure 4.9 shows the cooling of the sample plate. By keeping a constant temperature of the reference plate, two thermal time constants characterizing the heat flow in the calorimeter can be determined. Using eq. (2.41), we use the following fitting equation:

$$T_{sam}(t) = 70 + a(107.1323 - 70) \times \exp\left(-\left(\frac{t-734.321}{\tau_1}\right)\right) + b(107.1323 - 70) \times \exp\left(-\left(\frac{t-734.321}{\tau_2}\right)\right) \quad (4.1)$$

where  $t(0) = 734.321$  s and  $T_{sam}(0) = 107.1323$  mK denote the initial measurement time and initial sample temperature respectively,  $a$  and  $b$  denote the coefficients, which are both multiplied by the temperature difference between the initial temperature of the plate and the ambient (and equilibrium) temperature and which add up to 1 for a perfect fit,  $T_{sam}(\infty) = 70$  mK has been chosen as equilibrium temperature (since  $T_{ref} = 70$  mK during the whole measurement), and  $\tau_1$  and  $\tau_2$  denote the two time constants.

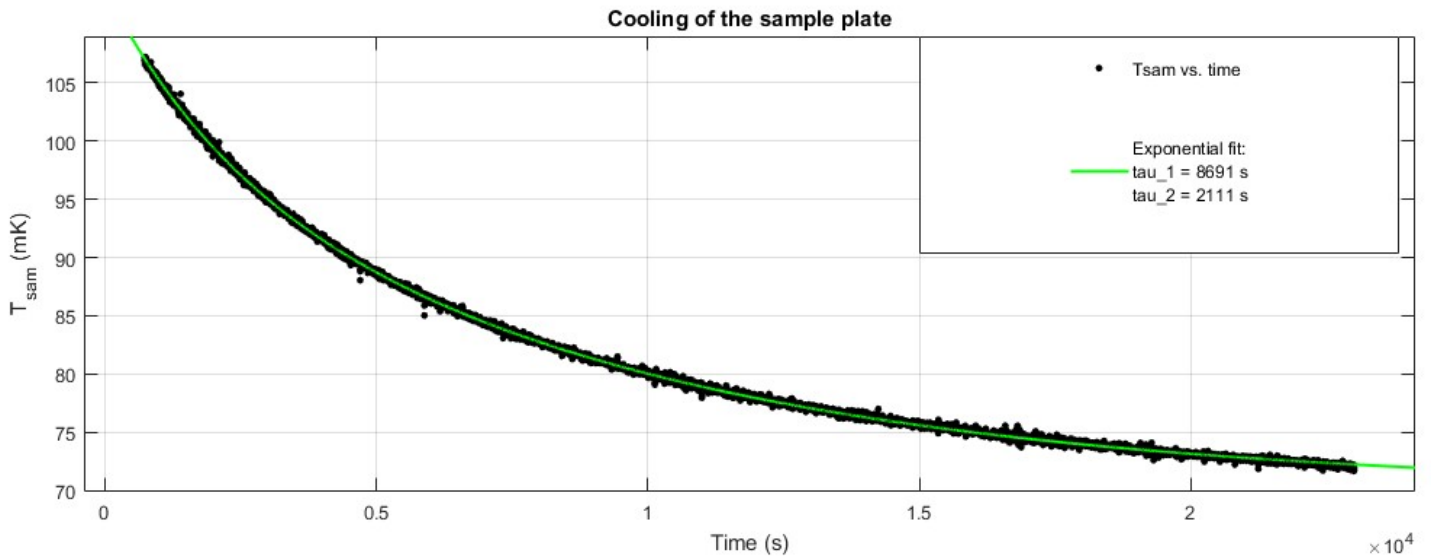


Figure 4.9. Fit of eq. (4.1) to the measured temperature of the sample, which temperature dropped in an exponential way. With coefficients  $a = 0.7758$  and  $b = 0.2232$ , their sum  $a + b = 0.9990$  is close to 1, indicating a good fit to the measured data.

We find  $\tau_1 \equiv \tau_{att} = 8691$  s and  $\tau_2 \equiv \tau_{sam} = 2111$  s, where we have attributed the largest time constant to that of the 3 dB attenuator, as the sample plate was designed to enable fast heat transfer and the attenuator could be poorly thermalized. Possibly, microwave attenuators have a higher temperature when dissipating power [34]. An overview of both time constants for all three runs is given in fig. 4.10 and fig. 4.11. In order to use the calorimeter to measure the dissipated power of the 3 dB attenuator when turned on,  $\tau_{att}$  needs to be much lower than the thermal time constants found for this run.

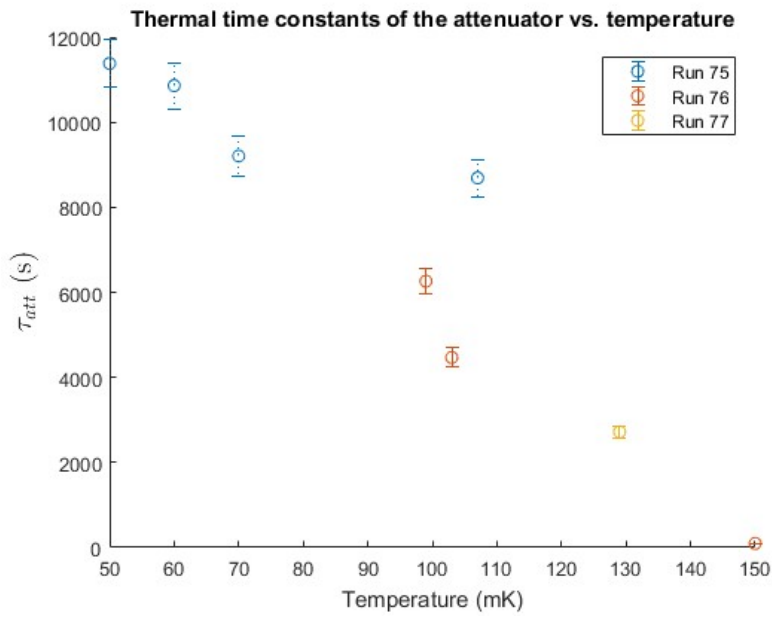


Figure 4.10. Overview of all measured thermal time constants of the attenuator during the three runs of the calorimeter. Error bars of 5% originate from the maximum error that follows from the fitting function and procedure in MATLAB. The attenuator appears to be better thermalized in runs 76 and 77. The general trend is that the thermal time constant decreases for increasing temperatures.

In the second and third run (runs 76 and 77) a newly fabricated 3 dB attenuator, designed to conduct heat faster to the sample plate, is used. As can be seen in fig. 4.10, the resulting thermal time constants are indeed lower than in the first run. However, in the last two runs the temperature of the reference plate was higher than 56 mK, which made measurements of  $\tau_{att}$  at lower temperatures impossible. The time constants depend on the (sample) temperature, as was expected from the discussion of the temperature-dependent thermal properties in section 3.2. Due to the large error associated with extrapolating these properties for lower temperatures, we are not able to calculate in which way the time constants depend on the temperature. However, the general trend is that  $\tau_{att}$  decreases for increasing temperatures.

The thermal time constants of the sample plate, as obtained from the fits, all have a smaller value than those of the attenuator (fig. 4.11). Again, we see that they are temperature-dependent, but we can only suggest that  $\tau_{sam}$  might increase with temperature if the sample plate is made of brass, and decrease if the sample plate is made of copper.

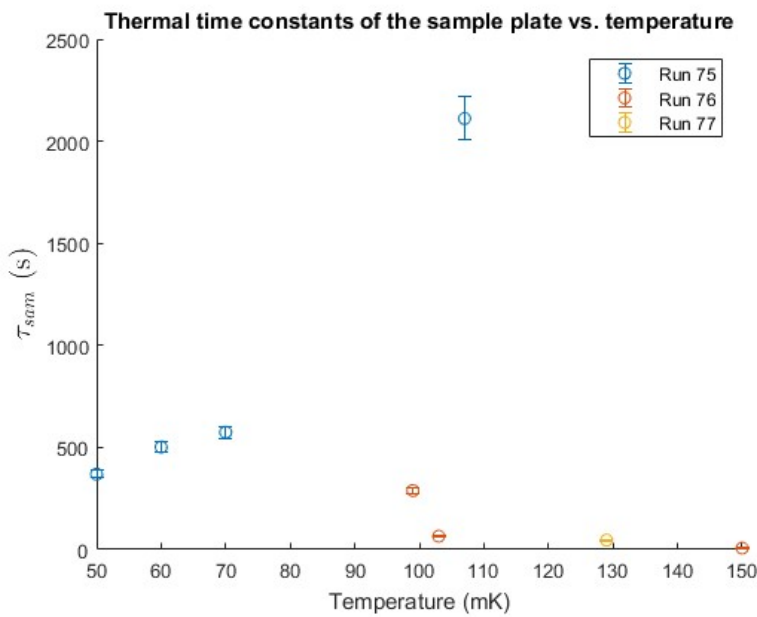


Figure 4.11. Overview of all measured thermal time constants of the sample plate during the three runs of the calorimeter. Error bars of 5% originate from the maximum error that follows from the fitting function and procedure in MATLAB. The sample plate appears to be better thermalized in runs 76 and 77.  $\tau_{sam}$  might increase with temperature if the sample plate is made of brass, and decrease if the sample plate is made of copper.

A possible explanation for the observed higher thermal time constants than those calculated in 3.2 might be that the thermal contacts have a higher thermal resistance in reality.

In conclusion, measurements done at higher temperatures show that the time constants of both the attenuator and the sample plate are reduced. This means that if the working temperature of the calorimeter can be reduced, the goal of having a characterized calorimeter with reasonably long thermal time constants is achieved, enabling an accurate measurement of the power dissipation of a 3 dB attenuator and that of a TWPA in the future as well.

## 5 Conclusion & Outlook

### Conclusion

This thesis describes some of the steps of a feasibility study that is required before conducting the proposed interferometer experiment with traveling wave parametric amplifiers (TWPAs), which could be able to falsify the existence of spontaneous wave function collapse using the visibility of the interference pattern as. The main question was if the interference visibility was still large enough to be observed for a TWPA gain of 20 dB and an insertion loss of 4 dB.

To this end, calculations on the visibility of the interference pattern are carried out by running Python programs with the QuTiP module on multiple computer infrastructures, thereby varying the gain and insertion loss of a TWPA in the proposed experiment. Visibilities as a function of amplification up to  $\kappa=1.7$  (13.4 dB gain) have been calculated when the effect of insertion loss on the interference visibility is excluded. While following an  $N^4$  dependence for the required amount of RAM, the limiting factor turned out to be the `int32` type used for the indices in the compressed sparse row (CSR) matrices in the QuTiP module.

The effect of dissipation in the TWPAs on the visibility for insertion losses up to 6.5 dB and visibilities for amplifications up to  $\kappa=0.6$  (3.5 dB gain) have been calculated. While the density matrices used in the same solver of the master equation follow an  $N^8$  dependence for the required amount of RAM, the program was again limited by the `int32` type for CSR indices. By doing Monte Carlo (MC) simulations and running each program with the same parameters multiple times, we have collected statistics resulting in visibilities for amplifications up to  $\kappa=0.8$  (5.3 dB gain). The visibilities calculated by the Master Equation (ME) solver lie within the confidence intervals of those calculated by the MC solver.

A cryogenic calorimeter is characterized to determine the length of the thermal time constants of its components. Measurements on the times constants of both the sample and the heat bath have led to the conclusion that the attenuator was not well thermalized. In the two follow-up experiments, presumably a parasitic power prevented the temperature of the heat bath to drop to that of the mixing chamber. However, measurements done at higher temperatures show that the time constants of both the attenuator and the sample plate are reduced. This means that if the working temperature of the calorimeter can be reduced, the goal of having a characterized calorimeter with reasonably long thermal time constants is achieved, enabling an accurate measurement of the power dissipation of a 3 dB attenuator and that of a TWPA in the future as well.

### Outlook

For further calculations of the expected interference visibilities for a higher TWPA gain, we need to consider the limitations of the ME and MC solvers, being the QuTiP internals and required amount of computational time respectively. The issue with the integer type of the CSR matrices has been reported to the QuTiP developers, with the result that this module will be updated in the future to support these as well. It is not possible to predict whether this will be done within the time frame of the research. If so, it is expected that the calculations of the visibilities for amplifications up to  $\kappa=2.0$  (16.1 dB gain) when excluding losses and visibilities for amplifications up to  $\kappa=0.7$  (4.4 dB gain) when including losses can be extended using the ME solver on the high memory node with 2 TB RAM available.

We are able to extend the calculations that include the effect of losses on the interference visibility by running Monte Carlo simulations on the Lisa Cluster in the future. At the moment of writing, access to this system has been granted with a budget of 100,000 core hours. We expect that this amount of computation time is sufficient to do these calculations for  $\kappa=0.9$  (6.2 dB gain). It might be an interesting alternative to calculate the interference visibilities for  $\kappa>0.9$  as well, while reducing the number of Monte Carlo trajectories for each value of  $\kappa$ . In that case, the calculations can be done for higher TWPA gains, which comes with the price of larger error bars (following the discussion in section 2.2.2).



## Bibliography

1. Romero-Isart, O. et al. (2010). Toward quantum superposition of living organisms. *New Journal of Physics*, *12*. (2010).
2. Gerlich, S. et al. Quantum interference of large organic molecules. *Nat. Commun.* *2*, (2011).
3. Bassi, A., Lochan, K., Satin, S., Singh, T. P. & Ulbricht, H. Models of wave-function collapse, underlying theories, and experimental tests. *Rev. Mod. Phys.* *85*, 471–527 (2013).
4. Bassi, A. Models of spontaneous wave function collapse: What they are, and how they can be tested. *J. Phys. Conf. Ser.* *701*, (2016).
5. Rademaker, L., van der Reep, T. et al. The Instability of a Quantum Superposition of Time Dilations. (2014). *arXiv:1410.2303v1*
6. Reep, T. H. A. van der, Le Large, X. G. A. & Oosterkamp, T. H. Studying spontaneous collapse of the wave function using two travelling wave parametric amplifiers. *Manuscript* (2018).
7. Adler, S. L. & Bassi, A. Collapse models with non-white noises. *J. Phys. A Math. Theor.* *40*, 15083–15098 (2007).
8. Bahrami, M., Smirne, A. & Bassi, A. Role of gravity in the collapse of a wave function: A probe into the Diósi-Penrose model. *Phys. Rev. A - At. Mol. Opt. Phys.* *90*, 1–8 (2014).
9. Hornberger, K. et al. Theory and experimental verification of Kapitza-Dirac-Talbot-Lau interferometry. *New J. Phys.* *11*, (2009).
10. White, T. C. et al. Traveling wave parametric amplifier with Josephson junctions using minimal resonator phase matching. *Appl. Phys. Lett.* *106*, (2015).
11. O'Brien, K., Macklin, C., Siddiqi, I. & Zhang, X. Resonantly phase-matched Josephson junction traveling wave parametric amplifier. 1–8 (2014).
12. Johansson, J. R., Nation, P. D. & Nori, F. QuTiP: An open-source Python framework for the dynamics of open quantum systems. *Comput. Phys. Commun.* *183*, 1760–1772 (2012).
13. Nation, P. D. & Johansson, J. R. QuTiP: Quantum Toolbox in Python. 241 (2014).
14. H. P. Breuer and F. Petruccione. *The Theory of Open Quantum Systems*. (Oxford University Press, 2002).
15. Macklin, C. et al. A near-quantum-limited Josephson traveling-wave parametric amplifier. *Science* (80-. ). *350*, 307 (2015).
16. Mølmer, K., Castin, Y. & Dalibard, J. Monte Carlo wave-function method in quantum optics. *Josa B* *10*, 524–538 (1993).
17. Dum, R., Parkins, A.S., Zoller, P., Gardiner, C. W. Monte Carlo simulation of master equations in quantum optics for vacuum, thermal and squeezed reservoirs. *Phys. Rev. A* *46*, 4382–4396 (1992).
18. Koehler, E., Brown, E. & Haneuse, S. J. P. A. On the assessment of Monte Carlo error in simulation-based Statistical analyses. *Am. Stat.* *63*, 155–162 (2009).
19. Incropera, F. P., DeWitt, D. P., Bergman, T. L. & Lavine, A. S. Fundamentals of Heat and Mass Transfer. *US Patent 5,328,671*, 257-261 (2007). doi:10.1073/pnas.0703993104
20. O'Sullivan, C. T. Newton's law of cooling—A critical assessment. *Am. J. Phys.* *58*, 956–960 (1990).
21. Bachmann, R. et al. Heat capacity measurements on small samples at low temperatures. *Rev. Sci. Instrum.* *43*, 205–214 (1972).
22. Kajastie, H. Loss measurements on superconducting Nb by a cryogenic dual compensated calorimeter for the implementation of the kilogram standard by the levitation mass. (2008). doi:10.1088/0026-1394/45/1/010
23. Gmelin, E. Modern low-temperature calorimetry. *Thermochim. Acta* *29*, 1–4 (1979).
24. Lasance, C. J. M. Ten years of boundary-condition- Independent compact thermal modeling of electronic parts: A review. *Heat Transf. Eng.* *29*, 149–168 (2008).

25. Lineykin, S. & Ben-Yaakov, S. Analysis of thermoelectric coolers by a spice-compatible equivalent-circuit model. *IEEE Power Electron. Lett.* **3**, 63–66 (2005).
26. Obame Ndong, E., Gallot-Lavallée, O. & Aitken, F. Analytical heat transfer modeling of a new radiation calorimeter. *Thermochim. Acta* **633**, 56–68 (2016).
27. Domen, S. R. & Lamperti, P. J. A Heat-loss-Compensated Calorimeter : Theory , Design , and Performance \*. **78**, 595–610 (1974).
28. Bastiaans, K. M. Power dissipation of a type II superconducting microwire carrying large oscillating currents at low temperatures. *Master thesis* (2015).
29. Pobell, F. Matters and methods at Low Temperatures. (2007). doi:10.1007/978-3-540-46360-3.
30. Duthil, P. Materials properties at low temperature. *Cern Accel. Sch.* **18** (2013). doi:10.5170/CERN-2014-005.77.
31. Ewin, J. W. *Experimental Techniques for Low-Temperature Measurements*, 227 (Oxford University Press, 2006).
32. Marquardt, E. D., Le, J. P. & Radebaugh, R. Cryogenic Material Properties Database. *11th Int. Cryocooler Conf.* **12**, 1–7 (2000).
33. Åström, K. J. & Hägglund, T. Revisiting the Ziegler-Nichols step response method for PID control. *J. Process Control* **14**, 635–650 (2004).
34. Yeh, J. H., Lefebvre, J., Premaratne, S., Wellstood, F. C. & Palmer, B. S. Microwave attenuators for use with quantum devices below 100 mK. *J. Appl. Phys.* **121**, 1–8 (2017).
35. Feitelson, D., Rudolph, L. & Schwiegelshohn, U. *Lecture Notes in Computer Science. Extended Semantic Web Conference*, 44-60 (2011). doi:10.1007/3-540-68339-9\_34.

## Appendix A: Computer infrastructures

### Overview of the distributed computer systems

To do the calculations as described in section 2.2, we have made use of two different computer systems: the NovaMaris Cluster (at the Lorentz Institute, Leiden) and the High Performance Computing (HPC) Cloud, the latter being maintained by SURFsara. Details of their specific infrastructure and way of operating are given in this appendix. Next to this, a short description of the data processing is given.

Each version of the SPI program has been run in a Linux environment with Python 3 (Python 3.5.2 and higher). Version 4.2.0 of the QuTiP module has been used [12][13], which has been installed after the required packages NumPy (1.8+), SciPy (0.15+) and Cython (0.21+) have been installed as well. In order to initialize programs on the Maris Cluster and the Lisa Cluster, customized batch scripts have been submitted to Slurm (version 17.02.9), which is an open-source job scheduler that is able to manage the resources available on the systems [35]. The batch scripts contain options for allocating these resources, such as the node on which the program should run, the maximum available amount of RAM, the amount of available CPU's and the directories in which the output and the error file(s) should be stored. An example of a used batch script can be found in Appendix B.

The SPI programs using the ME solver have saved the variables of interest as .mat files, which have been opened by MATLAB R2017a. Here, a script processes the arrays after which the relevant figures can be created. For the SPI programs using the MC solver, however, we have used a different approach as multiple runs results in the same number of output files. After merging the output files with the same parameters and saving the resulting file with an .xls extension, the rows that contain the variables of interest have been imported as arrays. In this way, again the relevant figures have been created using a statistical approach.

### Maris Cluster

The Maris Cluster is a small computational cluster at the Lorentz Institute. Access is primarily given to the research groups that have purchased the machines (e.g. the Beenakker group), but it can be granted to other researchers within the institute as well. We are part of the latter group and have been granted a guest account. Strictly spoken, this account does not have the same privileges as a Beenakker account (i.e. access to all nodes, no maximum amount of allocated CPUs and no maximum amount of running jobs). However, by discussing the required resources for our jobs and aligning these needs with those of the other users, we have managed to make use of a fair amount of resources during this Master Project.

The configuration and specification of the relevant part of the cluster is summarized as follows:

- The playground partition, consisting of 19 nodes, each with 8 CPUs and 16 GB of RAM, and 24 nodes, each with 8 CPUs and 32 GB of RAM. The clock speeds of all processors in this cluster is 2 GHz.
- The computation partition, consisting of 13 nodes, each with 48 CPUs with a clock speed of 2.2 GHz and 128 GB of RAM, and 15 nodes, each with 64 CPUs (apart from two nodes with 48 CPUs) with a clock speed of 3.2 GHz and 128 (1x), 192 (2x), 256 (4x) and 512 (8x) GB of RAM.
- The compintel partition, consisting of 2 nodes, each with 96 CPUs with a clock speed of 2.1 GHz and 512 GB of RAM.

The other three partitions are the notebook, emergency and GPU partitions. The cluster is optimized for multithreading applications and embarrassingly parallel problems.

## HPC Cloud

The HPC Cloud is a virtualizing environment where a user is able to build his/her own cluster. We have access to d-node41, which is the 2 TB high memory node with 40 CPUs. We share this node with one other user and have been able to use 1.5 TB and 20 CPUs. This amount of resources can be adjusted in a flexible way, in consultation with the contact person of the HPC Cloud (Nuno Ferreira).<sup>3</sup>

---

<sup>3</sup> More details on the system can be found on <https://userinfo.surfsara.nl/systems/hpc-cloud>

## Appendix B: Quick start guide SLURM & Maris Cluster

In order to enable a future user of the described infrastructures with a basic knowledge of Linux to run his/her program as fast as possible, we give a guide of the essential elements. First, we give a table in which the commands in SLURM are listed that we have found of most use during our computations. Then, we describe how to access the Maris Cluster and how to build a Virtual Machine (VM) on the HPC Cloud. Finally, we provide the reader with some general tips on making use of the resources in an effective way.

**Table of SLURM commands**

Command	Purpose
<code>sinfo</code>	Quick view of available nodes
<code>scontrol show nodes</code>	Detailed information about all nodes
<code>sbatch [name of batch file]</code>	Submit a batch file to initiate a job
<code>squeue -u [username]</code>	List of all jobs
<code>scontrol show jobid -dd [JobID]</code>	Show status of job
<code>sacct --format JobID,jobname,NTasks,nodelist,MaxRSS,maxVMSize,AveRSS,AveVMSize,jobs=[JobID]</code>	Provides with information about completed jobs
<code>scancel [JobID]</code>	Cancel job
<code>scancel -u [username]</code>	Cancel all jobs of a certain user
<code>scancel [JobID]</code>	Cancel job with specific JobID
<code>ls .   wc -l</code>	Count the amount of files within directory
<code>grep -rnw '[path name]' -e '[pattern]</code>	Search for files with a particular string in name
<code>find . -name "[string pattern]" -size 1000c delete</code>	Delete files with a particular string in name and larger than 1000 bytes

Table B1.

### Access to the Maris Cluster

Once granted access to the cluster, a user can login to its head node to access it. When starting with a Windows OS, one can use PuTTY<sup>4</sup>, a secure shell (SSH) client that is able to establish the two required connections (tunnels). The first tunnel leads to Styx, a platform with a Linux OS, while the second tunnel is used to connect with the Maris Cluster itself. It is not possible to SSH directly to the nodes, because of security reasons.

At the cluster itself, it is recommended to store all data in the `/marisdata/[username]` path instead of in the home directory, as there is a 10 GB quota enforced on the latter. Next to this, it is advisable to maintain a clear structure when creating directories. In this way, the user is able to manage his/her data easily and a third party could find its way through the files as well.

Transferring data from Windows to the cluster and vice versa can be done with WinSCP, a file transfer protocol client that safely copies files between a local and remote computer. For example, WinSCP is used to upload the file to the Styx platform.

Then, in Styx, the command `'scp [filename] novamaris:/marisdata/[username]/[path to directory]'` is used to copy the file to the preferred directory on the Maris Cluster.

<sup>4</sup> See <https://helpdesk.strw.leidenuniv.nl/wiki/doku.php?id=linux:putty> for more details.

Submitting jobs on the cluster should be done with a batch file. This is a script that contains the command to run the program and the required environment definitions. An example of such a batch file, with explanation given as comments, given below:

```
#!/bin/env bash

##comment out lines by adding at least two '#' at the beginning

#SBATCH --job-name=job_example      #this name will be listed in the list of submitted jobs

#SBATCH --account=guests

#SBATCH --partition=computation      #should be the name of the partition of the node

#SBATCH --array=1-200                #runs this job 200 times (with the same resources)

#SBATCH --output=/marisdata/lelarge/qutip_files/out+err/example_dir/%A_%a_output_file_name.out

#SBATCH --error=/marisdata/lelarge/qutip_files/out+err/example_dir/%A_%a_error_file_name.err

#SBATCH --time=3-23:00:00           #forces the program stop after 3 days and 23 hours

#SBATCH --mem=50000                  #a maximum amount of 50,000 MB is available for this job

#SBATCH --ntasks-per-node=1

#SBATCH --cpus-per-task=2           #if the program uses multithreading, multiple CPUs can be used

#SBATCH -w mariso60 #specifies on which nodes the program should run (here node o60) #SBATCH --no-queue

#SBATCH --mail-type=BEGIN

#SBATCH --mail-type=END              #sends an email when the program is finished

#SBATCH --mail-type=FAIL

#SBATCH --mail-user=user@example.com

##export OMP_NUM_THREADS=2          #should be the same as in --cpus-per-task

##export MKL_NUM_THREADS=2          #should be the same as in --cpus-per-task

/usr/bin/python3 /marisdata/lelarge/qutip_files/my_program

# /usr/bin/python3 picks makes sure that the right version of
Python is used to run the program listed in the absolute path
mentioned hereafter. Note the space in between. Make sure that
the batch file and program are both in the same directory.
```

Table B2.

## Appendix C: Additional results

All raw and processed data can be found on the \\datao2 drive at LION in the folder 'Xavier' with clear subdirectories.

### Master Equation solver

As discussed in section (2.2.1), a finite dimension of the Hilbert space that is created in the program leads to a truncation error. With the criterion stated in eq. (2.18), we have found an empirical estimate of the maximum value of kappa for a given dimension N (fig. x). For higher values of kappa, the truncated Hilbert space results in idler visibilities with an offset larger than 0.10%.

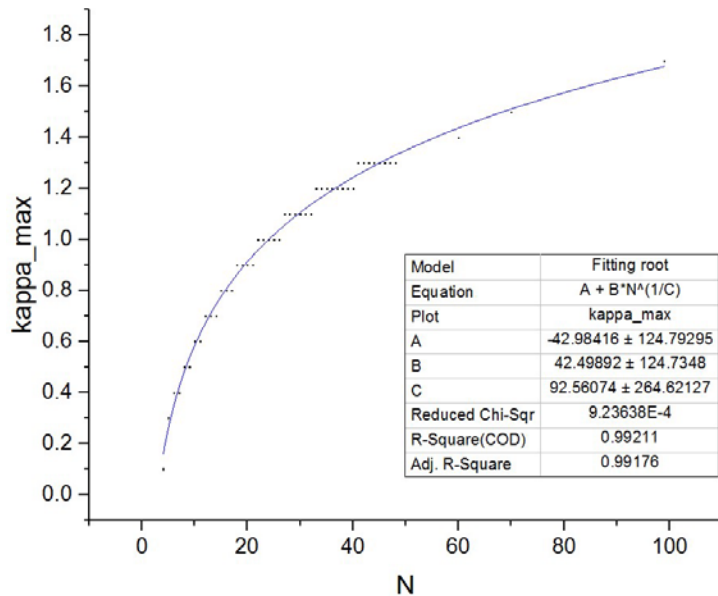
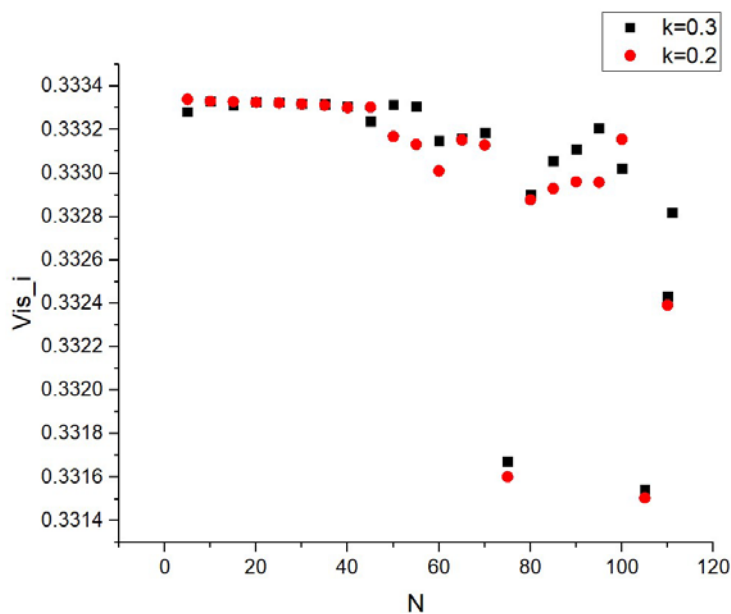


Figure C1. The maximum value of kappa that can be calculated for a given dimension of the Hilbert Space N, due to the truncation error as defined in eq. (2.18). For increasing kappa, a much higher dimension N is needed.



However, a strange feature that occurs for  $N > 40$  is found (fig. x). First we assumed that higher dimensions of the Hilbert space would result in computed visibility values that converge to the analytical ones, as these would approach an infinite Hilbert space. The reality is that some dips in the visibility occur for higher N, which can increase the relative error to values as high as 0.55% for  $N = 105$ . For higher values of kappa, the errors seem to be reduced for the same N. The origin of this feature is yet unknown.

Figure C2. Idler visibilities calculated for certain values of N, showing that for increasing N dips may occur that can result in errors that are even larger than the truncation error.

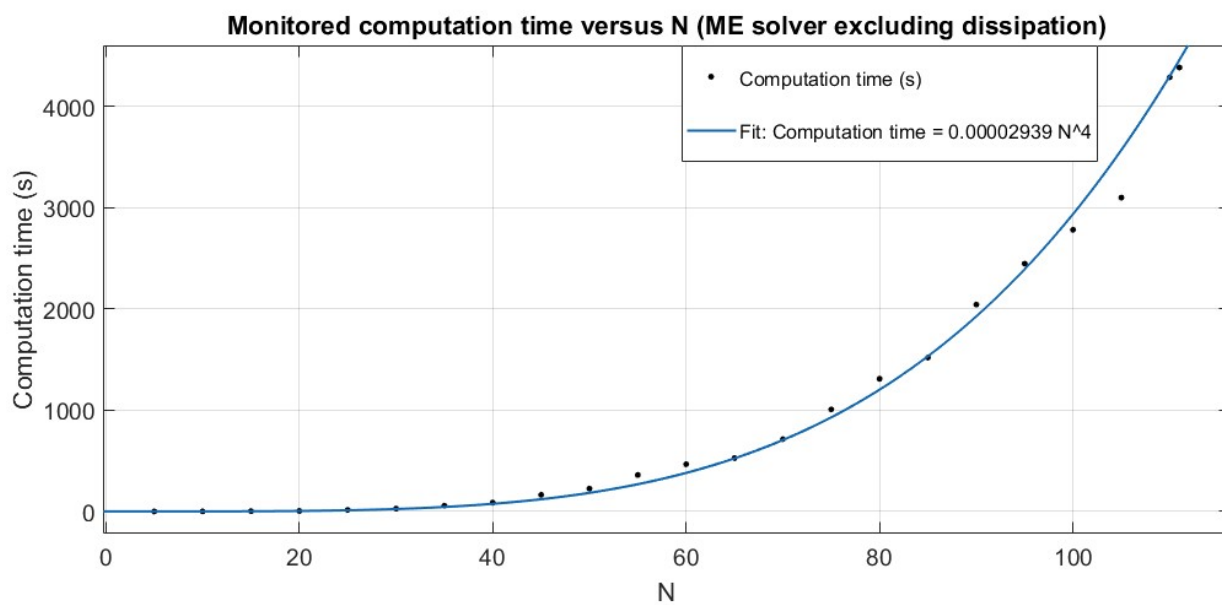


Figure C3. Computation time required for the ME solver excluding dissipation as a function of N, showing again an  $N^4$  dependence. Deviating points are due to the varying load on the nodes of the cluster.

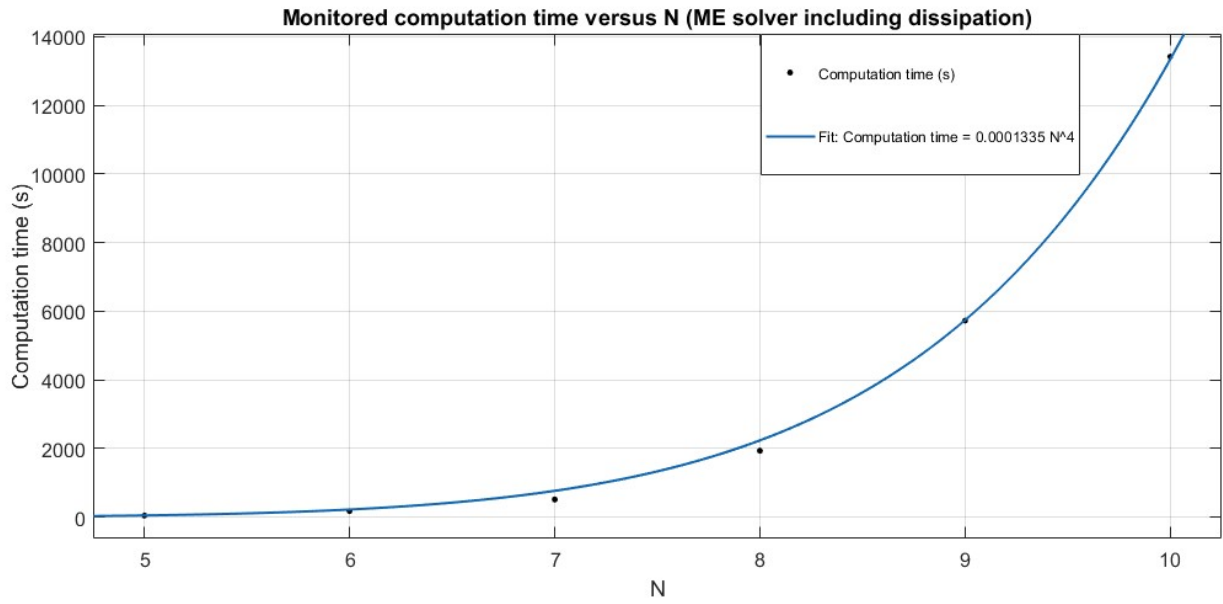


Figure C4. Computation time required for the ME solver including dissipation as a function of N, showing again an  $N^4$  dependence.

Table C1 combines the results of figure 4.2 with the empirical formula of fig. C1 for one loop step to extrapolate for higher kappa. It can be seen that the required amount of RAM when running the ME solver is extremely large for higher values of kappa.

$\kappa_{\max}$	N	RAM (MB)	Computation time (h)
1.7	104	102,994	0.9
1.8	127	229,031	2
1.9	157	534,907	4
2.0	193	1,221,544	11
2.1	236	2,731,040	25
2.2	290	6,226,901	56
2.3	356	14,140,997	128
2.4	437	32,107,448	290
2.5	536	72,667,328	657

Table C1.

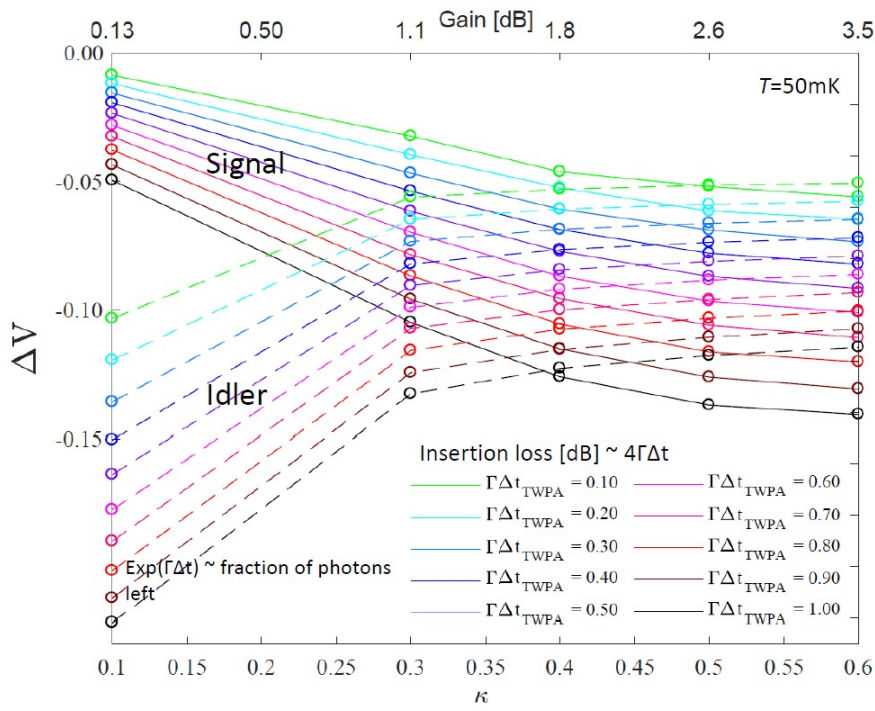


Figure C5. Difference with analytical visibility appears to converge to a constant value, which is promising if it's not possible to compute for all kappa's.

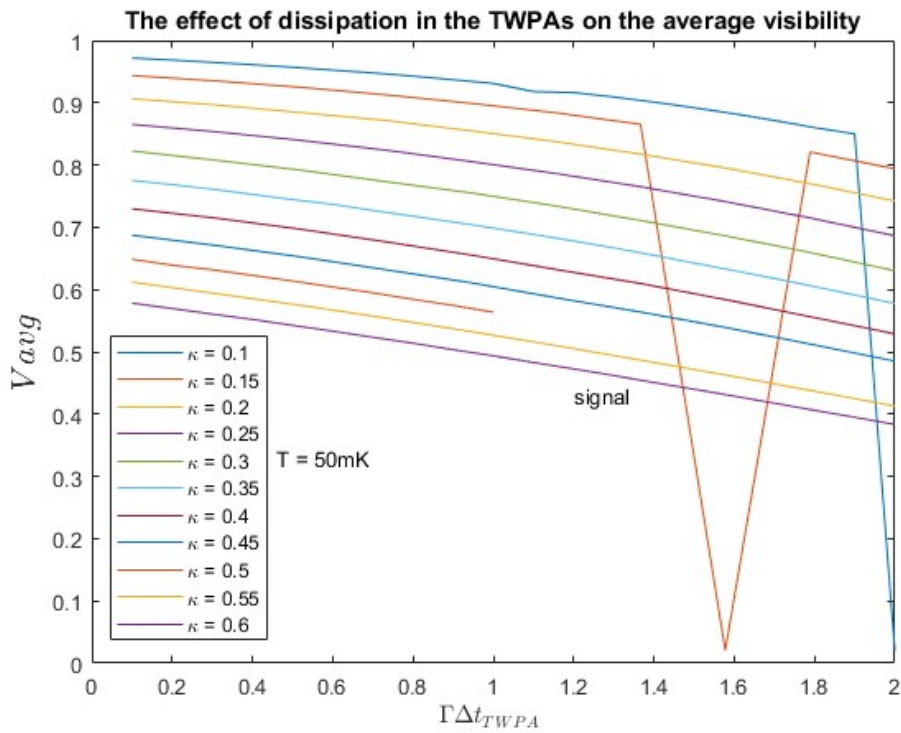


Figure C6. ME solver visibility as a function of losses, plotted for multiple values of kappa. The dips show that bugs might appear within the calculations.

## MC solver

### MC solver: statistics

Histogram of the calculated signal visibilities for  $N=8$  and 2,000 paths, showing a Gaussian distribution. Running the program multiple times with the same parameters (job array) decreases the relative error

Figure C7. Optimization problem which led us to calculate the visibilities with the MC solver with 2,000 paths for  $\kappa = 0.7 - 0.9$  and  $N=12, 15$  and  $18$  respectively.

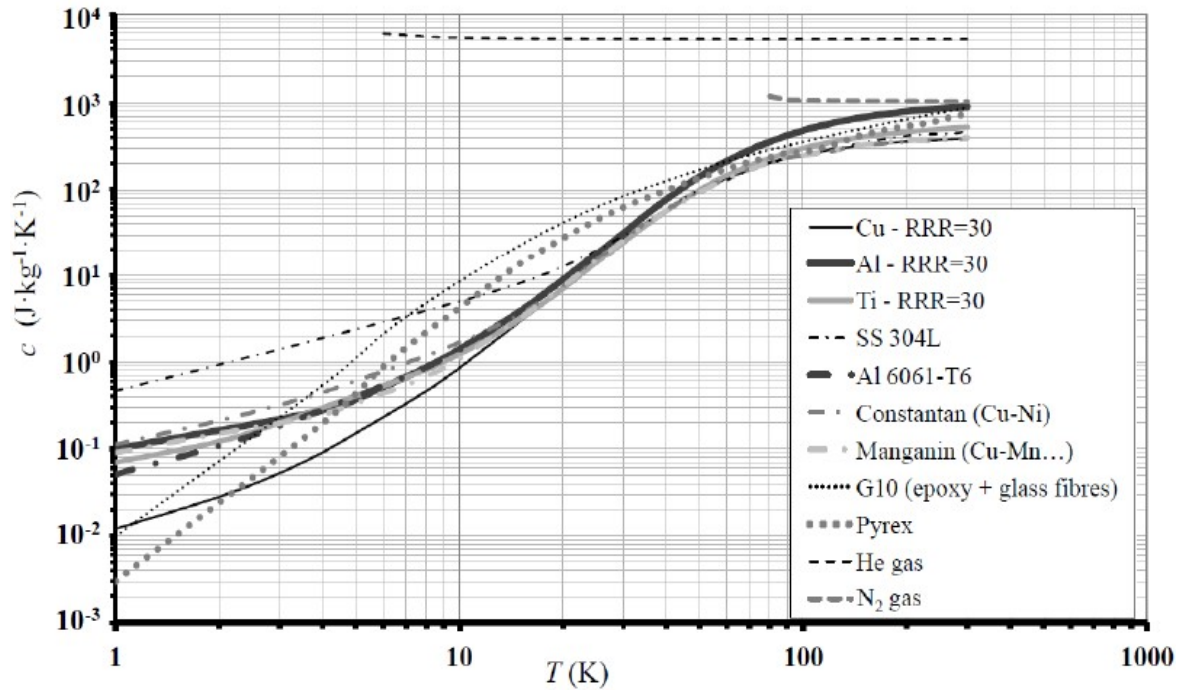
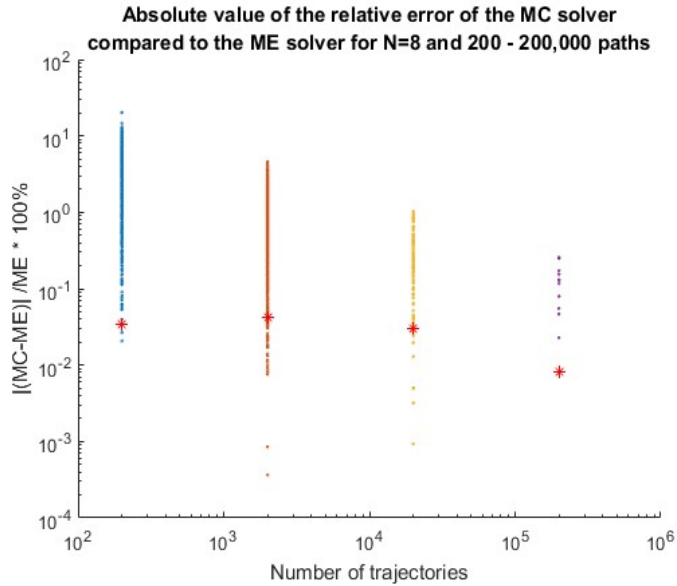


Figure C8. Specific heat capacity for various materials at temperatures between 1 - 300 K. We use this graph to extrapolate this property for stainless steel (SS) to 30 mK. Figure taken from [30].

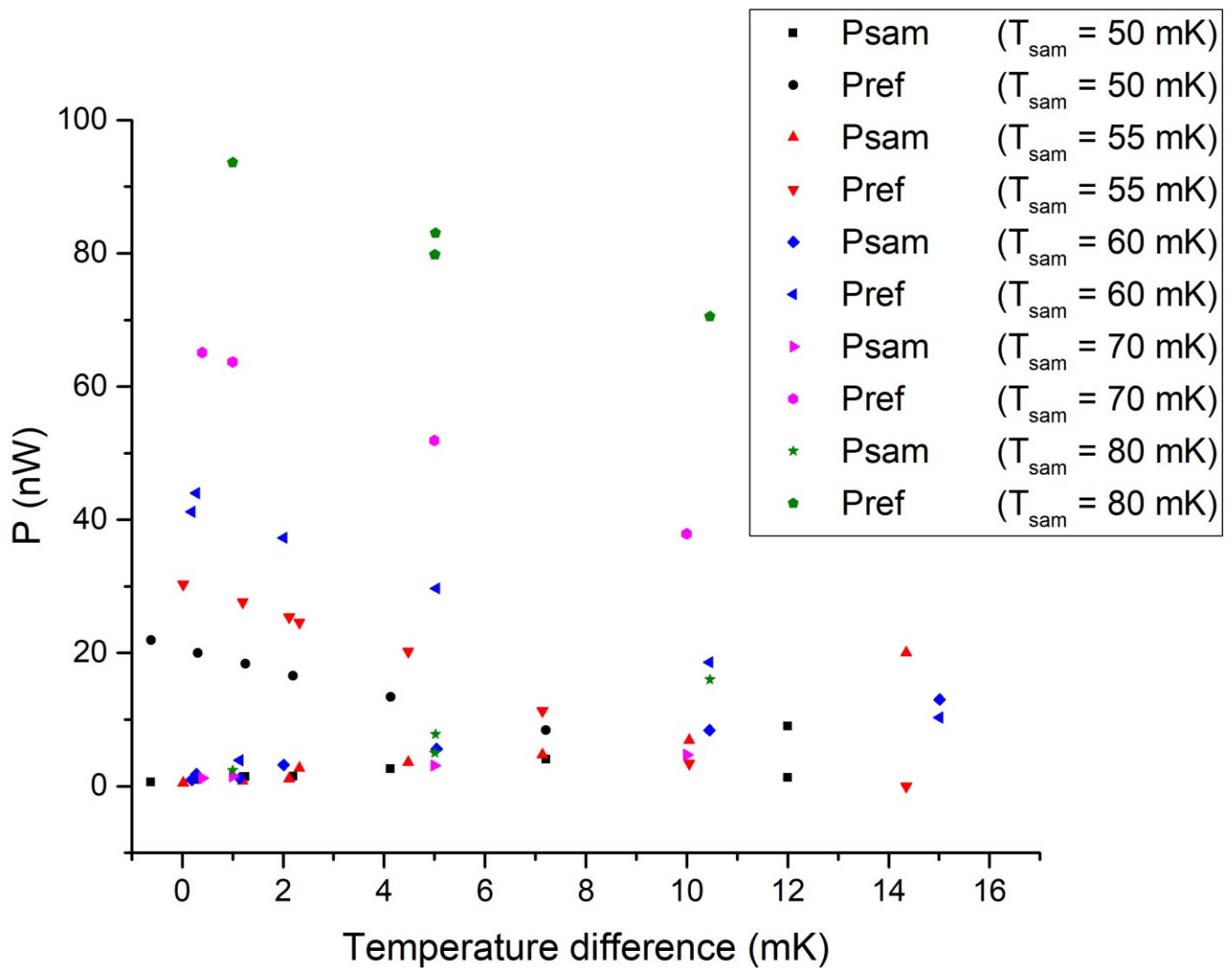


Figure C9. The magnitude of amount power to maintain the set temperatures for both the sample and the reference plate depends on the temperature difference between these set temperatures.

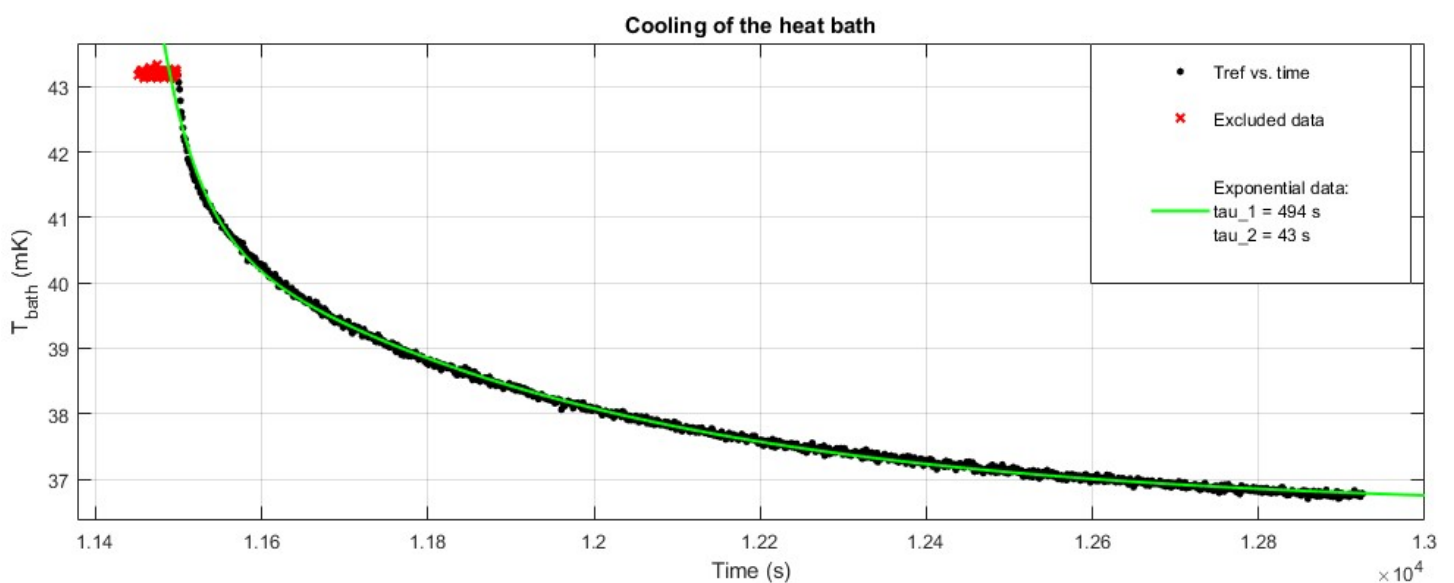


Figure C10. Cooling of the heat bath. Again an exponential fit is used to determine the two remaining time constants.

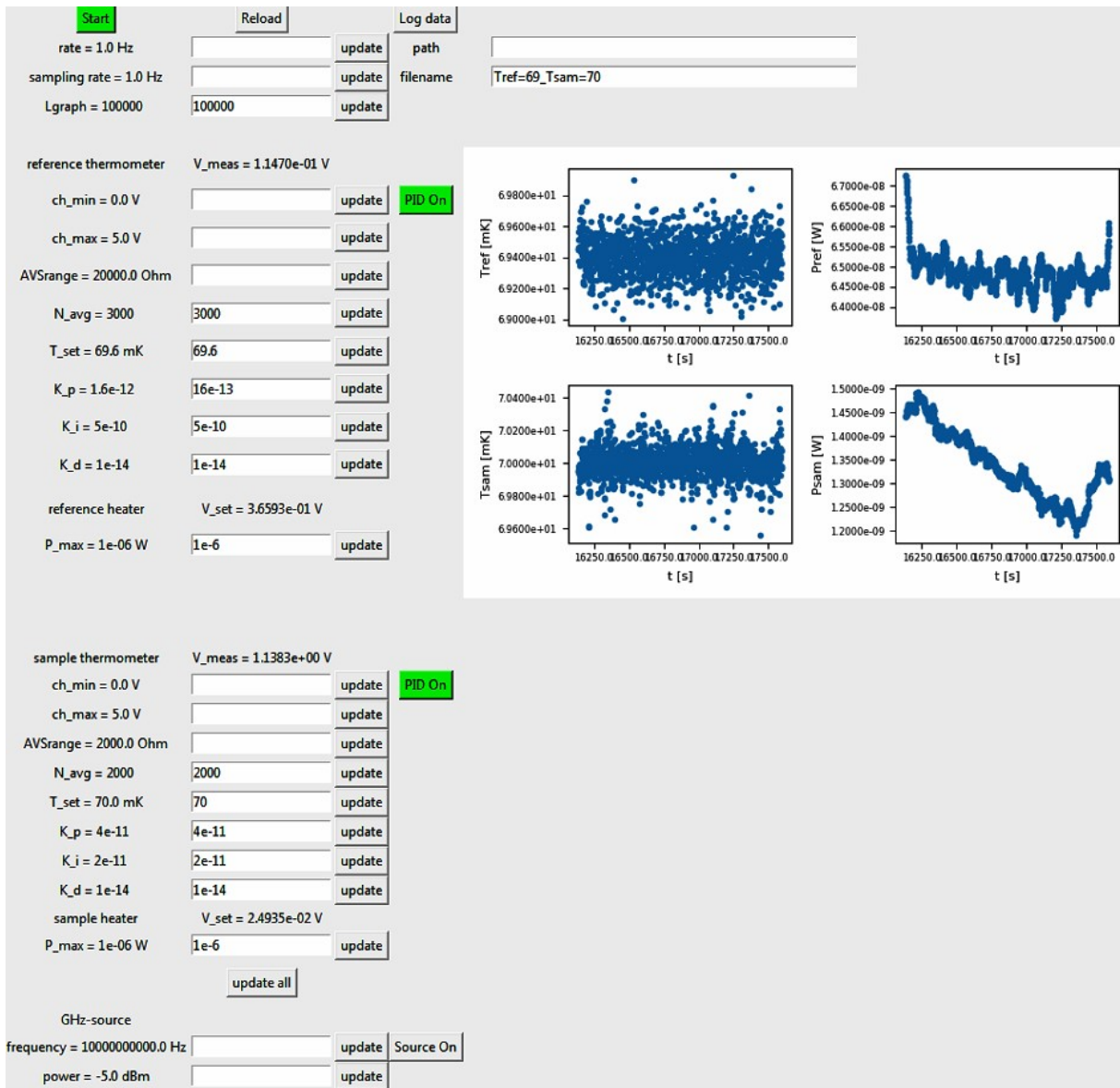


Figure C11. Overview of the Calorimeter.py program, used to measure the temperature of the sample plate and reference plate, enable PID control and turn on the microwave attenuator.